S. P. Kárason
M. A. Srinivasan
A. M. Annaswamy

Department of Mechanical Engineering
Massachusetts Institute of Technology
Cambridge, Massachusetts 02139, USA

Encoding and Decoding of Static Information in Tactile Sensing Systems

Abstract

Human and robot tactile sensing can be accomplished by arrays of mechanosensors embedded in a deformable medium. When an object comes in contact with the surface of the medium, information about the shape of the medium's surface and the force distribution within the region of contact on the surface is available in the stress/strain states at the sensor locations within the medium. The mechanosensors transduce these signals, and the problem for the central processor is to reliably and efficiently infer the contact state and the object properties on the surface from the sensor signals. In this paper, a frequency-domain approach is used to solve the problem of encoding and decoding mechanosensory information. A solution to the encoding problem is given with the medium modeled as a general three-dimensional infinite half-space composed of a linear elastic material and subjected to three-dimensional loads. It is shown that considerations of symmetry and bandwidth of sensor response uniquely determine the optimal stress/strain components the sensors need to transduce. It is further shown how the decoding leads to an ill-posed problem, and how that problem can be efficiently solved in the frequency domain using a regularized inverse such as the multivariate Wiener inverse. The results are then applied to the encoding and decoding of contact with a shaped object. It is shown that the solution can also be used in pseudodynamic problems, such as the estimation of the onset of slip.

1. Introduction

Manual exploration and manipulation of objects in an environment is important to both humans and robots. Human performance of these tasks is enabled by the haptic system, consisting of tactile and kinesthetic sensory systems together with a motor-control system. Similar classification is applicable to the sensory and motor systems of robots. A detailed and quantitative understanding of the underlying dynamics, information flow, and control strategies will benefit investigations of both human haptics and the development of machine haptics. It is especially valuable in the development of haptic interfaces through which humans can interact manually with teleoperated systems or computer-generated virtual environments (Srinivasan 1995). Although the principles of operation for human-made devices are quite different from those of humans, the constraints on the performance of these haptic tasks, such as the laws of physics governing the mechanics of contact and the presence of friction and gravity, are the same for both. In addition, the type of tactual sensory information, their processing, and the computation of the required control action are sufficiently similar for the two systems that the common aspects of information processing can be functionally separated from the hardware implementations. Therefore a computational theory of haptics that investigates what kind of information is necessary, and how it has to be processed to successfully complete a desired haptic task can be common to humans and robotic systems.

It has been recognized for some time that robots with dextrous hands need "tactile sense" to successfully explore and manipulate objects in their environment. Reviews of the various tactile sensor designs have been given by several authors (see for example Nicholls 1992; Shimoga 1992; Jayawant 1989). Because of the natural constraints imposed by this mode of sensing, the engineering designs have had to follow nature in overall configuration. By definition, tactile sensing is achieved through direct contact with objects, and therefore a "skin" is necessary to protect the sensors from physical damage. The requirements that the skin should be soft comes from the needs to have (1) regions of contact within which skin surface conforms to the object surface (instead of point or line contact that occurs between two rigid objects), and (2) significant deformation within the medium so that the sensors are activated and have enough resolution. If the substrate material on which the sensors and the skin rest is also soft, then, in addition to the above, better prehension stability can be achieved. The facts that a point contact has no torsional resistance and its stability is highly sensitive to local aberrations imply that compliant skin gives better prehension. Thus, although robotic tactile sensors themselves might differ in their operation, depending upon whether they

The International Journal of Robotics Research
Vol. 18, No. 2, February 1999, pp. 131-151,

respond to changes in conductance, capacitance, contact area, light intensity, etc., within each sensing cell caused by local mechanical distortions, the overall configuration of all the designs is that of mechano-sensitive transducers embedded in a deformable medium.

Two stages in tactual information processing, *encoding* and *decoding*, make up the *identification problem*, which is so called because it involves the determination of the state of the object and its relationship to the tactual sensory system. The system discussed here differs in some ways from traditional dynamic systems. The most prominent difference is that it has both spatial and temporal variables, whereas traditional lumped parameter systems only have temporal ones. In both natural and human-made tactile systems, the encoding process is the transduction of the mechanical stimulus into electrical signals that contain, in a coded form, information about the stimulus features. The inverse problem, i.e., the decoding process or the calculation of the surface shape or surface tractions from the transduced signals, is in many respects significantly more difficult. The encoding is essentially a low-pass filtering process that indicates that the decoding will be ill-posed in the sense that the higher-frequency components of the signals will be prone to noise contamination and special methods must be applied for successful decoding.

Several papers can be found in the robotics literature on the mechanistic modeling, encoding, and decoding of surface conditions from subsurface measurements using tactile sensors. The earlier papers dealt primarily with the mechanistic model and only the encoding. The problem is approached by Phillips and Johnson (1981) from a physiological point of view, and by Fearing and Hollerbach (1984) from a robotic point of view. Both papers use the plane-strain assumption, and give solutions to the two-dimensional (2-D) encoding problem. The decoding problem is first addressed by Srinivasan (1988) and Pati et al. (1988), both of which solve only the 2-D plane-strain case. Srinivasan (1988) uses a frequency-domain approach, whereas a neural network approach is used by Pati and colleagues (1988). The plane-strain assumption is dropped by Cameron, Daniel, and Durrant-Whyte (1988), but the analysis is limited to the properties of a specific photoelastic sensor. In work by Fearing (1990), again plane stress or plane strain is assumed, and the effects of finite thickness as well as the stability of the grasp are investigated. Rossi and coworkers (1991) investigated the mathematics of the decoding problem using matrix-regularizing operators, where the loading is assumed to be axisymmetric. The combined results of the above papers are detailed by Fearing (1992); this work is the most thorough treatment so far on the infinite half-space and analytical solutions of the encoding and decoding problems. Fearing (1992) further gives the three-dimensional (3-D) half-space solution only to a normal point load in the appendix. Additionally, finite element analysis is used by Speeter (1992), where the effects of shear loads on subsurface strain and stress are demonstrated graphically, and also by Ellis and Qin (1994) in an investigation of the differentiation of shapes and the inherent difficulties that arise because of the blurring effect of the skin. In work by Howe and Cutkosky (1993), the encoding and decoding of a stress-rate sensor are investigated and a scalar Wiener inverse is suggested for the decoding. Nicolson and Fearing (1993) give the 2-D plane-strain solution for a cylindrical finger. Shimojo (1997) uses the finite-element method to investigate the mechanical filtering effects of an elastic layer over sensors placed on an elastic foundation, with the conclusion that even the thinnest elastic layer causes considerable spatial low-pass filtering of stress distribution at the sensor location.

In summary, none of the above papers treats either the encoding or the decoding problem fully. Until now, all the results published on the reconstruction of general surface loads and profiles from subsurface tactile signals do not solve the full 3-D problem. The effects and interactions of shear loads and the selection of appropriate sensor signals have not been investigated. In addition, neither has the decoding problem been fully addressed, or has the multivariate Wiener inverse been applied. In this paper, we address mainly the mechanistic modeling, encoding, and decoding problems. The contributions of this paper can be itemized as follows:

- A complete solution to the 3-D half-space problem is given for arbitrary 3-D static loading conditions and any linearly elastic material, instead of the 2-D solutions previously used. The solution also applies to pseudo-dynamic problems that can be described as a sequence of elastostatic problems (such as the estimation of the onset of slip).
- The solution is formulated using transfer-function matrices in the domain of spatial frequency, which allows us to look at the qualitative properties and general behavior of the solution, irrespective of particular cases of the loading or object shape. It also enables efficient numerical implementation based on the theory of linear signal processing.
- Symmetry and signal-bandwidth arguments are invoked to select the optimal transducing signals or types of sensors. For decoding, we can then apply the signal-processing and regularization theory in a manner similar to what has been done in the development of computational theory of vision.
- Numerically stable, multivariate, regularizing solution methods for the decoding problem are delineated. The ill-posedness of the decoding process is analyzed, and we show how the extensively developed methods of image restoration can be applied to avoid the problems associated with the ill-posedness.

In Section 2, we formulate and solve the 3-D half-space elastic model, which serves as a description of the encoding process. For the sake of clarity, the mathematical expressions are detailed in the appendix. In Section 3, we analyze the

decoding problem, first as an ideal problem without any real-world effects such as noise, following which we incorporate the effects of sampling and random additive noise into the solution. This constitutes an algorithm for the decoding process. In Section 4, we give example numerical simulations of the methods proposed in Section 3. Conclusions are given in Section 5.

2. The Encoding Problem

From a theoretical viewpoint, tactile-sensor response to any given stimulus can be predicted if we have the following:

1. a mechanistic model of the deformable medium, which can be used to calculate reliably the stresses and strains at each point in the medium for a given mechanical stimulus; and
2. a model of the sensor that provides the relationship between the relevant stimulus, i.e., a particular combination of stresses and strains in the local neighborhood of a sensor that it is responsive to, and the sensor response.

For example, an appropriate mechanistic model of the human skin and the soft tissues underneath enables us to investigate one of the important questions in cutaneous neurophysiology: identifying the relevant stimulus that causes each receptor type to respond (Phillips and Johnson 1981; Srinivasan and Dandekar 1996).

2.1. Mechanistic Analysis

In the robotic tactile-sensing literature, contact-analysis problems are frequently simplified by posing them as 2-D plane-strain problems in the elastic half-space (Sneddon 1951; Gladwell 1980; Johnson 1985). The surface load or profile is then assumed not to change along one dimension on the planar surface; for example, as in the case of a line load. Almost all the results in the literature on the analysis of tactile sensing have made this assumption. Clearly, this is a serious limitation. In this section, we give the more general solution when 3-D loads are arbitrarily distributed over the contact region.

The assumption that the problem can be posed as a contact problem in the semi-infinite half-space still remains, mainly for the sake of analytical tractability. We can, however, partially justify that assumption, based on numerical solutions obtained for finite models (Dandekar 1995; Srinivasan and Dandekar 1996), which show that the effects of finite extent are minimal when the contact region is small relative to the surface area of the medium. The semi-infinite half-space solution is a good approximation in such cases, because the stress-strain response to a load decreases rapidly with distance from the load.

The problem is set up so that the boundary surface coincides with the xy-plane and the positive z-axis points into the medium (see Fig. 1). The material is assumed to be linearly elastic and homogeneous. It is also assumed to extend to infinity in both negative and positive x-, y-directions and in the positive z-direction. The surface load is described by the traction-vector field $f(x, y) = [f_x(x, y),\ f_y(x, y),\ f_z(x, y)]^T$ and the surface-displacement field as $u_0(x, y) = [u_x(x, y, 0),\ u_y(x, y, 0),\ u_z(x, y, 0)]^T$. In our formulation, the boundary conditions can be forces, displacements, or mixed, i.e., when any three elements from both f and u_0 are given. We intend to present the solution in the space of spatial frequencies and use transfer functions to simplify solutions and gain further insight.

2.2. Transfer-Function Matrices (TFM)

Many equivalent routes to the solution of the encoding problem exist, but the simplest and most direct way for our purposes is to transform the fundamental differential equations of equilibrium and the stress-strain relationship equations (Generalized Hooke's law) using the Fourier transform over (x, y)-space. Examples of this approach can be seen in the works of Eason, Fulton, and Sneddon (Eason, Fulton, and Sneddon 1956; Sneddon 1975). The derivation of the transfer-function matrix form of the solution is given in the appendix. Similar to what is done in control theory, we employ here the concept of a transfer-function matrix (TFM). The transfer-function matrices we give here have the Fourier transform of the components of either $f(x, y)$ or $u_0(x, y)$ as the inputs, and any displacements, strains, or stresses in the medium as the outputs. Each entry of the TFM would then correspond to the contribution of a particular input component to the corresponding output component. For example the entry in the TFM for the z-displacement resulting from the x-load, or $u_z^x(x, y, z)$, we would write

$$\bar{u}_z^x(\omega_x, \omega_y, z) = T_{u_z^x f}(\omega_x, \omega_y, z)\bar{f}_x(\omega_x, \omega_y)$$

to obtain the Fourier transform $\bar{u}_z^x(\omega_x, \omega_y, z)$ of $u_z^x(x, y, z)$ from the transfer function $T_{u_z^x f}(\omega_x, \omega_y, z)$ and the Fourier transform $\bar{f}_x(\omega_x, \omega_y)$ of the surface-shear load $f_x(x, y)$. Here, ω_x and ω_y correspond to spatial frequencies in the x- and y-directions, respectively. Then we can write

$$\begin{aligned} &\bar{u} = T_{uf}\bar{f}, \quad \bar{\varepsilon} = T_{\varepsilon f}\bar{f}, \quad \bar{\sigma} = T_{\sigma f}\bar{f}, \quad \bar{p}_n = T_{p_n f}\bar{f}, \\ &\bar{u} = T_{uu_0}\bar{u}_0, \quad \bar{\varepsilon} = T_{\varepsilon u_0}\bar{u}_0, \quad \bar{\sigma} = T_{\sigma u_0}\bar{u}_0, \quad \bar{p}_n = T_{p_n u_0}\bar{u}_0, \end{aligned} \tag{1}$$

where the subscript f indicates that surface tractions are inputs and the subscript u_0 indicates that surface displacements are inputs. As an example, we give here $T_{\varepsilon u_0}$, i.e., the case when the surface displacements (u_0) are the inputs and the subsurface strains (ε) are outputs (the other TFMs are given in the appendix):

$$T_{\varepsilon u_0} = \frac{e^{-z\Omega}}{(3-4\nu)\Omega} \times \begin{bmatrix} j\omega_x\left((3-4\nu)\Omega - \omega_x^2 z\right) & -j\omega_x^2\omega_y z & \Omega\omega_x^2 z \\ -j\omega_x\omega_y^2 z & j\omega_y\left((3-4\nu)\Omega - \omega_y^2 z\right) & \Omega\omega_y^2 z \\ -j\Omega\omega_x(1-\Omega z) & -j\Omega\omega_y(1-\Omega z) & -\Omega^2(2(1-2\nu)+\Omega z) \\ \frac{j}{2}\omega_y\left((3-4\nu)\Omega - 2\omega_x^2 z\right) & \frac{j}{2}\omega_x\left((3-4\nu)\Omega - 2\omega_y^2 z\right) & \Omega\omega_x\omega_y z \\ -\frac{1}{2}\left((3-4\nu)\Omega^2 + \omega_x^2(1-2\Omega z)\right) & -\frac{1}{2}\omega_x\omega_y(1-2z\Omega) & j\Omega\omega_x(1-2\nu)+\Omega z) \\ -\frac{1}{2}\omega_x\omega_y(1-2z\Omega) & -\frac{1}{2}\left((3-4\nu)\Omega^2 + \omega_y^2(1-2\Omega z)\right) & j\Omega\omega_x(1-2\nu)+\Omega z) \end{bmatrix}, \quad (2)$$

where $\Omega = \left(\omega_x^2 + \omega_y^2\right)^{1/2}$, μ is the shear modulus, and ν is the Poisson ratio. For mixed cases, TFMs can also be easily constructed by choosing appropriate elements from the TFMs above.

2.3. *Mixed Boundary-Value Problems*

There are four distinct cases in the formulation of the TFMs for the half-space problem, which can be described as follows:

1. only displacement inputs or traction inputs are specified over the entire surface;
2. displacement and traction inputs are mixed, but the same inputs are specified over the entire surface;
3. displacement and traction inputs are mixed, but different combinations of inputs are specified within and outside a known contact region; and
4. the same type of inputs as in point 3, but the contact region is unknown.

The statements in eq. (1) represent the solution for the encoding problem in case 1, because given $f(x, y)$, or $u_0(x, y)$ over the entire surface, we can predict $u(x, y, z)$, $\varepsilon(x, y, z)$, $\sigma(x, y, z)$, and $p_n(x, y, z)$. If the relevant stimulus, i.e., a particular combination of stresses and strains in the local neighborhood of the sensor to which it is responsive, is known, we can predict the sensor response as well. For example, if the sensor response is linearly related to the strain ε_{zz}, then it is the relevant stimulus for that sensor. On the other hand, if the relevant stimulus needs to be identified, we can use eq. (1) to generate hypotheses that can be tested against the empirically measured sensor response, as is done by Phillips and Johnson (1981) and Srinivasan and Dandekar (1996).

For case 2, the solution can be computed using the underlying TFM, which can be found as follows: expressing an arbitrary input vector ϕ_0 in $\mathbb{R}^3$ as a linear combination of displacements u_0 and tractions f, we get

$$\overline{\phi}_0 = F\begin{bmatrix} \overline{u}_0 \\ \overline{f} \end{bmatrix},$$

where F has rank 3. Using the TFM $T_{u_0 f}$ between the input f and output u_0, we get

$$\overline{\phi}_0 = FT'_{\phi_0 f}\overline{f} \triangleq T_{\phi_0 f}\overline{f},$$

$$\text{where} \quad T'_{\phi_0 f} = \begin{bmatrix} T_{u_0 f} \\ I \end{bmatrix}.$$

Since both F and $T'_{\phi_0 f}$ have rank 3, it follows that $T_{\phi_0 f}$ can be inverted to obtain $T_{f\phi_0}$. Substituting $\overline{f} = T_{f\phi_0}\overline{\phi}_0$ in eqs. (14)–(18) in the appendix, we can solve this type of mixed boundary-value problem. Alternately, the input u_0 can be used instead of f by employing the TFMS in eqs. (19)–(23).

In cases 3 and 4, if analytical solutions are available for the subsurface variables, then a similar procedure as in case 2 can be carried out to select the appropriate TFMs that correspond to the specified inputs and desired outputs. In the absence of analytical solutions, numerical procedures need to be followed. For example, in case 3, assume that either the contact region or total load is known and that at every point a collection of three independent tractions or displacements is known (and hence the remaining three are unknown). The set of possible surface tractions and displacements can then be divided into two subsets, ϕ_{0_1} and ϕ_{0_2}, three components in each. The surface of the medium can be divided, similarly, into two mutually exclusive regions A_1 and A_2, such that in A_1, ϕ_{0_1} is known but ϕ_{0_2} is unknown, whereas in A_2, the converse is true. Also, using the TFMs $T_{u_0\phi_0}$ and $T_{f\phi_0}$, we can obtain the TFMs $T_{\phi_{0_1}\phi_{0_2}}$ and $T_{\phi_{0_2}\phi_{0_1}}$. We can then apply the following algorithm:

1. At every point on the surface, estimate the unknown parts (using perhaps a known analytical solution that is close to the unknown numerical solution).
2. Using $T_{\phi_{0_1}\phi_{0_2}}$ together with the initial guess for ϕ_{0_2} (which is known in A_2 and estimated in A_1), obtain a new estimate for ϕ_{0_1} in A_2. Similarly, obtain a new estimate for ϕ_{0_2} in A_1.
3. Iterate the estimated inputs ϕ_{0_1} in A_2 and ϕ_{0_2} in A_1 by enforcing the known inputs as in step 2.

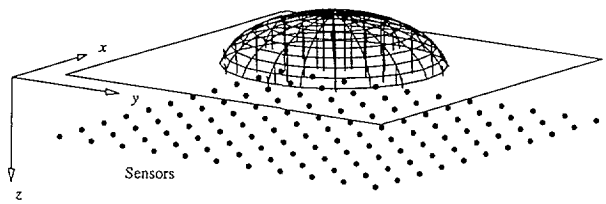

Fig. 1. The semi-infinite half-space with surface tractions and subsurface sensors. The x- and y-dimensions extend to infinity in both negative and positive directions. The z-dimension extends from 0 to positive infinity. The tractions are distributed over the contact area, each point being subjected to three-dimensional loading, $f(x, y) = [f_x, f_y, f_z]^T$.

If the contact region is also unknown, which corresponds to case 4 above, an iterative estimation procedure must be used for the contact region as well, which can be carried out employing information on object shape and total load. In Section 4, an illustrative example of this case is considered and the above algorithm is applied. While we do not carry out a formal analysis of this algorithm, linearity and Parseval's theorem (total energy in frequency and spatial space is equal) can be called upon to establish the conditions under which successive iterations (as in step 3) give improved solutions.

3. The Decoding Problem

Tactile information is obtained with mechanosensors embedded in a deformable medium that is in contact with a shaped object. Mechanosensors, embedded within the medium, can at best provide information on skin-surface shape and surface-traction distribution. From this information, contact region, shape of the object, and contact state need to be inferred. The problem at hand is therefore the decoding; i.e., reconstruction of the surface shape of the medium, the tractions on the surface as well as the region of contact from subsurface mechanosensory information.

The approach we have chosen is to represent the solution in the spatial frequency domain, in terms of transfer functions as in eq. (1). Equivalently, using superposition of the point-load solution, the solutions can also be presented as convolution integrals. However, the transfer-function approach gives solutions whose properties are more transparent, and some important statements can be made regarding their qualitative properties (such as the symmetry and bandwidth properties of subsurface stress or strain components), irrespective of the exact form of the loading. This approach also enables the use of efficient tools of linear signal processing, such as the fast Fourier transform. This section is organized as follows. In Section 3.1, we discuss the constraints that the task of tactile identification puts on the selection and the number of necessary sensor signals, and furthermore identify possible candidates of sensor-signal combinations. In Section 3.2, we use symmetry arguments to analyze the TFMs of the previously identified candidates to find an optimal combination. Finally, in Section 3.3, we show how an optimal multivariate Wiener inverse can be used to reconstruct the surface signals from measurements of the sensor signal in the presence of noise and sampling errors.

3.1. Sensory Information Necessary for Reconstruction

The most obvious signals to reconstruct are the deformed shape of the surface of the medium and the spatial distribution of surface tractions. Discontinuities in slope or curvature of surface shape do not reliably indicate contact borders, as an object surface within the contact region could have similar discontinuities and therefore be mistakenly identified as borders of the contact region. Each of the regions where the surface tractions (e.g., normal pressure) are nonzero indicates the region of contact with the object. Within these regions, the object shape is the same as the shape of the deformed medium surface. In addition, the surface-traction distribution can directly give valuable information on the stability of grasp and the type of contact, be it static or vibrating.

Some interesting properties of the TFMs can be obtained when dynamic systems theory is applied to them. In what follows, we assume that the sensors pick up a strain component or mean normal stress, and further, that the components of the strain are expressed in the global coordinate system (x, y, z). If the medium is incompressible, uniform normal pressure on its surface does not cause any strains within. Therefore, measurements of strains only are not sufficient to fully reconstruct surface-force distributions, as the mean normal stress component will not be detectable in the strains for incompressible materials. This is the main reason for the use of the mean normal stress as a variable that needs to be sensed.

If no shear loads are present, or if the relationship between normal and shear loads is known, only one component of strain needs to be sensed. However, if shear independent of the normal load is present, the more-general TFM formulation must be employed, as the surface tractions must be obtained by the inversion of some of the statements in eqs. (15) and (17) in the appendix. What and how many components of the strain tensor are needed depend on the assumptions we make on the loading conditions. This can be detailed in the following cases.

1. *No shear loading.* In this case, the normal pressure distribution and surface displacements need to be reconstructed. Sensing of any strain or the mean normal pressure is generally sufficient, but the need for rotational symmetry about the z-axis makes either p_n or ε_{zz} the natural choice. Using p_n will enable the calculation of the uniform pressure component of the total load, which no combination of strains can provide if $\nu = 0.5$ (i.e., incompressible material). However, the combination of

p_n and ε_{zz} can also be used to obtain increased spatial frequency bandwidth (see Section 3.2.2), in addition to obtaining the full load distribution.

2. *Relationship between normal loads and shear loads is fully or partially known.* This is the case, for example, if the object is sliding in an unknown direction over the surface under Coulomb friction conditions, or if the relationship between normal and shear loads is unknown but the direction of the shear load is known. Then any two subsurface stress and strain components need to be sensed to fully reconstruct all three surface-traction or displacement components, and a natural choice would again be p_n and ε_{zz} as above.
3. *All tractions unknown.* All three traction components and surface displacements need to be reconstructed. Considering only combinations symmetric in (x, y), the following combinations become candidates:

   (a) $(\varepsilon_{xy}, \varepsilon_{xx}, \varepsilon_{yy})$,
   (b) $(\varepsilon_{xx}, \varepsilon_{yy}, \varepsilon_{zz})$,
   (c) $(\varepsilon_{zz}, \varepsilon_{xz}, \varepsilon_{yz})$,
   (d) $(\varepsilon_{xy}, \varepsilon_{xz}, \varepsilon_{yz})$,
   (e) $(p_n, \varepsilon_{zz}, \varepsilon_{xy})$,
   (f) $p_n, \varepsilon_{xx}, \varepsilon_{yy}$, and
   (g) $(p_n, \varepsilon_{xz}, \varepsilon_{yz})$.

   We will show below how we can make an optimal choice among these component sets.

Case 3 is the most general one, and it indicates that any sensor population that is suitable for reconstructing arbitrary loading conditions must measure at least three independent stress-strain components (out of a total of six). More components could be used to get redundant measurements, and hence more-reliable estimates, but here we will only look at the minimal set.

3.2. Analysis of TFM Properties

We now try to use the properties of the TFM to identify the sensor combination that is most suitable for tactile sensing. In particular, we look at the rank of the TFM and its bandwidth.

3.2.1. Rank of the TFM

Since we intend to invert the TFM, we need to consider its rank, which is a key property and has to be full for an inversion to be possible. If the TFM loses rank, information is lost, as the output will span fewer dimensions than the input. The conditions under which the TFM loses rank are closely related to zero properties of dynamic systems, just as the conditions under which the TFM becomes infinite are related to the poles. The TFMs in our case are, however, always finite, and therefore do not possess any polelike properties, which is to be expected from a linear mechanical system in stable equilibrium. The TFM loses rank when its determinant becomes zero. When the traction vector f is the input, the determinants of the TFM candidates (see eq. (15) in the appendix) detailed in Section 3.1 are

$$\det(T_{\varepsilon_{xy},\varepsilon_{xx},\varepsilon_{yy}}) = 0 \quad \text{(a)}$$

$$\det(T_{\varepsilon_{xx},\varepsilon_{yy},\varepsilon_{zz}}) = -(1-2\nu)\frac{\omega_x\omega_y}{\Omega^2}e^{-z\Omega} \quad \text{(b)}$$

$$\det(T_{\varepsilon_{zz},\varepsilon_{xz},\varepsilon_{yz}}) = -(1-2\nu)e^{-z\Omega} \quad \text{(c)}$$

$$\det(T_{\varepsilon_{xy},\varepsilon_{xz},\varepsilon_{yz}}) = -(1-2\nu)\frac{\omega_x\omega_y}{\Omega^2}e^{-z\Omega} \quad \text{(d)}$$

$$\det(T_{p_n,\varepsilon_{zz},\varepsilon_{xy}}) = \frac{2(1+\nu)}{3}\frac{\omega_x^2-\omega_y^2}{\Omega^2}e^{-z\Omega} \quad \text{(e)}$$

$$\det(T_{p_n,\varepsilon_{xx},\varepsilon_{yy}}) = \frac{2(1+\nu)}{3}\frac{2\omega_x\omega_y}{\Omega^2}e^{-z\Omega} \quad \text{(f)}$$

$$\det(T_{p_n,\varepsilon_{xz},\varepsilon_{yz}}) = \frac{2(1+\nu)}{3}e^{-z\Omega}. \quad \text{(g)}$$

We see that the first one is always rank deficient. If the medium is incompressible, i.e., if $1-2\nu=0$, then the next three TFMs lose rank. As discussed in Section 3.1, the mean normal stress, p_n, must be included among the sensor signals in the case of an incompressible material. Otherwise, the component of the surface load that contributes to the mean normal stress cannot be reconstructed. A special case is a solid subjected to uniform pressure. No strains will be detected inside the solid, although the pressure can be arbitrary. We also note that the TFM loses rank for candidate (e) when $\omega_x = \pm\omega_y$ and for candidate (f) when $\omega_x = 0$ or $\omega_y = 0$. That the TFM loses rank for certain directions in the (ω_x, ω_y) plane means that the inputs cannot be reconstructed along those same lines. In the case of candidate (f), this means that the cumulative load distribution in either the x- or y-direction cannot be reconstructed. For example, if $\omega_y = 0$, in frequency space we have the traction vector $\bar{f}(\omega_x, 0) = \bar{g}(\omega_x)$, and $g(x) = \int_{-\infty}^{+\infty} f(x, y)dy$, which is the cumulative load distribution along x. Therefore, since the TFM for candidate (f) is rank deficient for $\omega_y = 0$, the component containing information on the cumulative distribution of the input along x will be lost in the encoding. The same arguments apply to candidate (e), with the coordinate system rotated by $\pm 45°$ about the z-axis. Candidate (g) is the only one that does not lose rank, and therefore has the desirable combination of p_n and strains that the sensors need to transduce for decoding.

REMARK 1. The comments above, which are made in the context of the traction vector f being the input, are also valid when the displacement vector u_0 or any combination ϕ_0 of tractions and displacements are the inputs. This is because when u_0 is the input, since the TFM that relates u_0 and f (eq. (18) in the appendix) has the determinant

$$\det T_{u_0 f} = \frac{2(1+\nu)^3}{3-4\nu}E^3\frac{1}{\Omega^3}, \quad (3)$$

it does not alter the rank properties of each of the TFMs of candidates (a)–(g) above. Similarly, when ϕ_0 is the input,

since $T_{f\phi_0}$ is invertible (see Section 2.3), the rank properties of these candidates still remain unaltered.

3.2.2. *Bandwidth of Spatial Frequency*

A frequently used property of dynamic systems is the bandwidth of the TFM, which measures how the attenuation of each signal in the medium depends on frequency. High bandwidth would mean that reconstruction is possible with finer details, and is therefore desirable. However, since the frequency is 2-D, the bandwidth will also depend on orientation in the (x, y)-plane, which in turn can be used to exclude sensor combinations that lack rotational symmetry about the z-axis. To compare the bandwidth of the various combinations (a)–(g) listed above, we look at the power spectrum of the TFMs, a line at a time. That is, the power spectrum of each sensor signal is the norm of the corresponding line vector in the TFM. For example,

$$\mathcal{P}_{\varepsilon_{xz}} = \| \left[T_{\varepsilon^x_{xz}} \; T_{\varepsilon^y_{xz}} \; T_{\varepsilon^z_{xz}} \right] \|^2.$$

The power spectrum for the possible sensory signals can be seen in Figures 2–7. The figures show the power spectrum as density plots with darker and lighter areas indicating frequencies where attenuation is low and high, respectively. Also shown along the border of the density plot are projected profiles of the power spectrum along the lines $\omega_x = 0$, $\omega_y = 0$, and $\omega_x = \omega_y$. Figures 2–7 show the power spectrum respectively for p_n, ε_{xx}, ε_{zz}, ε_{xy}, ε_{xz}, and candidate (g) $(\mathcal{P}_{p_n} + \mathcal{P}_{\varepsilon_{xz}} + \mathcal{P}_{\varepsilon_{yz}})$. We note that the power spectrums for ε_{yy} or ε_{yz} are obtained from those of ε_{xx} or ε_{xz}, rotated by 90°.

The two most important features of the spectrums are their frequency bandwidth and rotational symmetry. If the sensor responses cannot be combined to form a rotationally symmetric spectrum, the sensor response would depend on stimulus orientation in the xy-plane, which is undesirable because of different proportions of signal to noise. We note that $\mathcal{P}_{\varepsilon_{zz}}$ has a shape similar to $\mathcal{P}_{p_n}$ but higher bandwidth, while the other strains have orientation-dependent bandwidth. This excludes candidate (e), since for $\mathcal{P}_{\varepsilon_{xy}}$ (Fig. 5) frequencies along ±45° are attenuated. Candidate (f) is also excluded, because both ε_{xx} and ε_{yy} attenuate frequencies along 0 and 90°, and using both will therefore not produce rotational symmetry. It is worth noting that the directions of attenuation coincide with the conditions under which the TFM loses rank (see Section 3.2.1). Candidate (g) is therefore the only one remaining, and it can provide rotational symmetry, as seen in Figure 7. The importance of having full rank and bandwidth in all directions becomes apparent when one considers that loss of rank means that infinitely many load combinations produce identical sensor responses, and hence make inversion impossible for those cases, and lower bandwidth in any one direction means that less information on the spatial features characterizing that dimension of the object are observable by the sensors.

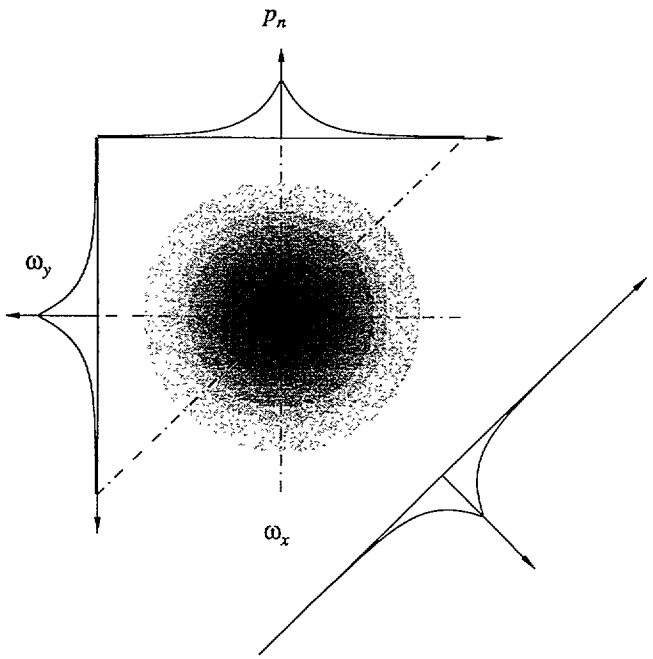

Fig. 2. The power spectrum of the mean normal stress $\mathcal{P}_{p_n}$. We observe that it is rotationally symmetric with a smaller bandwidth than $\mathcal{P}_{\varepsilon_{zz}}$ (shown in Fig. 4).

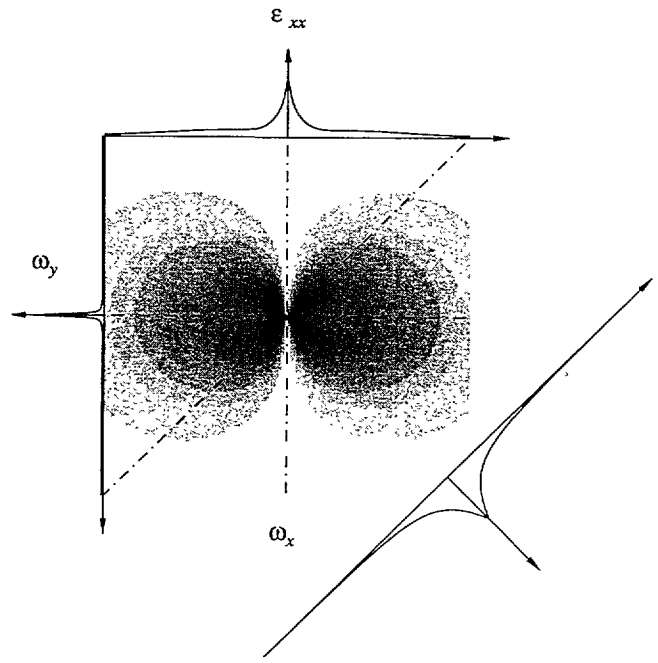

Fig. 3. The power spectrum of the x-normal strain $\mathcal{P}_{\varepsilon_{xx}}$. This power spectrum is not rotationally symmetric, as it behaves like $\mathcal{P}_{p_n}$ in the $\omega_x = \pm\omega_y$-directions, but as $\mathcal{P}_{\varepsilon_{zz}}$ in the ω_x-direction (along $\omega_y = 0$.)

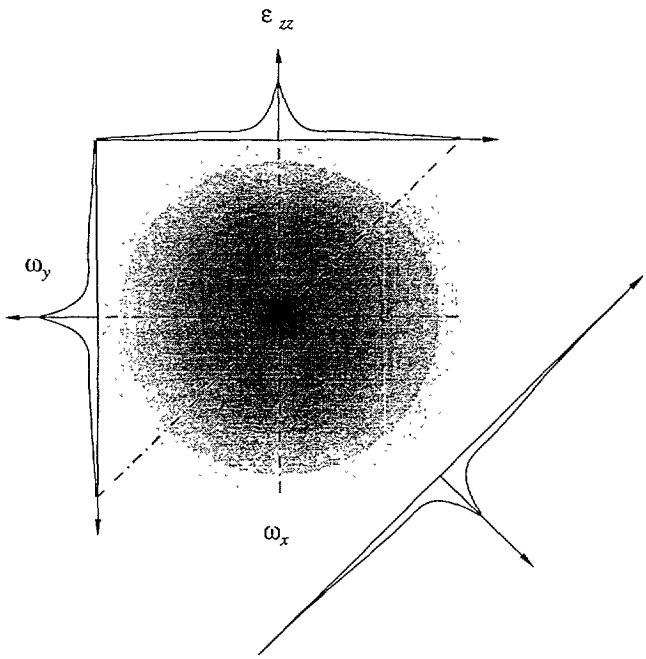

Fig. 4. The power spectrum of the z-normal strain $\mathcal{P}_{\varepsilon_{zz}}$. This one is also rotationally symmetric, as $\mathcal{P}_{p_n}$ in Figure 2, but it has higher bandwidth.

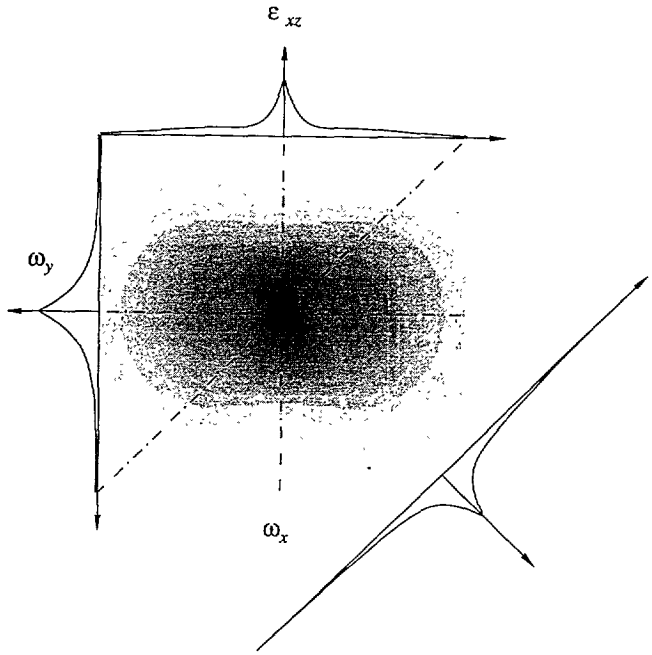

Fig. 6. The power spectrum of the xz-shear strain $\mathcal{P}_{\varepsilon_{xz}}$. This power spectrum behaves like $\mathcal{P}_{\varepsilon_{zz}}$ in the ω_x-direction, but as $\mathcal{P}_{p_n}$ in the ω_y-direction, and it is therefore not rotationally symmetric. The $\mathcal{P}_{\varepsilon_{yz}}$ power spectrum can be obtained from this one by a permutation of (x, y) or a rotation of the axis by $\pm 90°$.

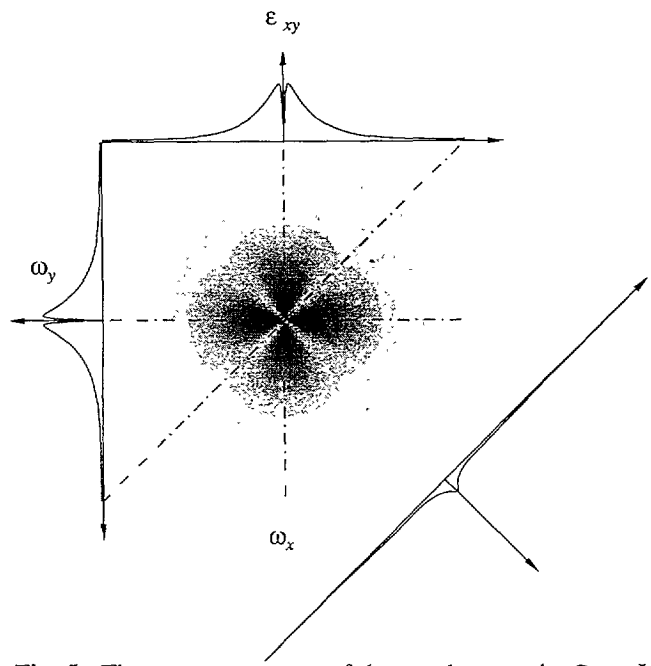

Fig. 5. The power spectrum of the xy-shear strain $\mathcal{P}_{\varepsilon_{xy}}$. It is not rotationally symmetric, and it differs from the other spectrums in that it has a sharp minimum at the origin.

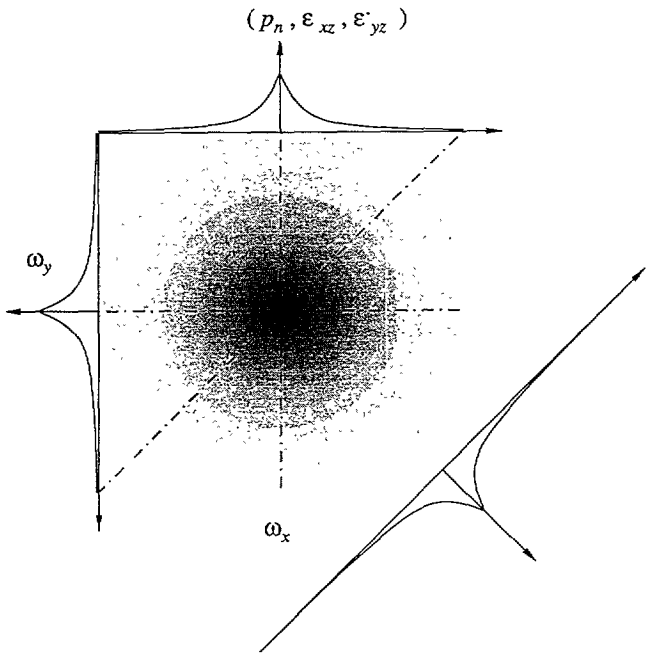

Fig. 7. The power spectrum of the sensor signals in candidate (g); i.e., $\mathcal{P}_{(p_n, \varepsilon_{xz}, \varepsilon_{yz})} = \mathcal{P}_{p_n} + \mathcal{P}_{\varepsilon_{xz}} + \mathcal{P}_{\varepsilon_{yz}}$. We observe that it is rotationally symmetric, since the ε_{xz}- and ε_{yz}-components complement each other and p_n is rotationally symmetric.

The conclusion is, therefore, that given the assumption that we are using Cartesian strain sensors, the only combination that works for incompressible materials and possesses symmetry is $(p_n, \varepsilon_{xz}, \varepsilon_{yz})$, and the TFM for that selection is (refer to the appendix)

$$T_{sf} = \frac{(1+\nu)e^{-z\Omega}}{E\Omega} \begin{bmatrix} -j\omega_x & -j\omega_y & \Omega \\ -(\Omega - \omega_x^2 z) & \omega_x\omega_y z & j\Omega\omega_x z \\ \omega_x\omega_y z & -(\Omega - \omega_y^2 z) & j\Omega\omega_y z \end{bmatrix}, \quad (4)$$

where s stands for a normalized sensor signal, $s = \left[\frac{3}{2E}p_n, \varepsilon_{xz}, \varepsilon_{yz}\right]^T$.

REMARK 2. The sensor combination $(\sigma_{zz}, \sigma_{xz}, \sigma_{yz})$ is equivalent to $(p_n, \varepsilon_{xz}, \varepsilon_{yz})$, but the latter combination can be considered to be unique and optimal because in sensors, strains are directly measured and stresses are inferred from the strains. Mean normal stress, p_n, is a better variable to measure than volumetric strain, since the latter is always zero for incompressible materials. As long as we are sensing stresses or strains, the range of spatial frequency sensed through each component is of the same order. But only some of the components and combinations are rotationally symmetric about the z-axis.

3.2.3. The Structure of the Sensor TFM

Analyzing the structure of the TFM in eq. (4), we observe that the $e^{-\Omega z}$ factor, which is common to all the terms, expresses how the signals get increasingly low-pass filtered or blurred with depth. It is a consequence of the model including the resistance of the medium to shear, and is therefore necessary if the sensors are to have a subsurface location. We further observe that there are two basic variants of transfer functions in the sensor transfer-function matrix, which we will call T1 and T2. While T1 is characterized by its norm behaving like $e^{-\Omega z}$ (for example $T_{p_n f_z} = e^{-\Omega z}$), T2 is characterized by its norm behaving like $|\omega_i| ze^{-\Omega z}$, $i = x, y$ (e.g., $|T_{\varepsilon_{xz} f_z}| = |\omega_x| ze^{-\Omega z}$).They differ in that the T1 transfer function has low-pass characteristics, but the T2 transfer function has band-pass characteristics. In the spatial domain, this means that the response of the T1 terms is spread over a larger area, since a predominantly low-frequency content indicates slow variations in the spatial domain. On the other hand, the response of the T2 terms is more localized, and they respond better to sudden changes in the loading since they have higher bandwidth. Terms like $j\frac{\omega_i}{\Omega}e^{-\Omega z}$, $i = x, y$, have the same bandwidth as the T1, but terms like $\frac{\omega_i\omega_k z}{\Omega}e^{-\Omega z}$, $i, k = x, y$ are of type T2.

The TFM is symmetric with respect to x and y, since the half-space model is identical for x and y. Looking at the TFM linewise, we see that line 1 (p_n terms) contains only T1 terms, but lines 2 and 3 (ε_{xz} and ε_{yz} terms) contain mostly T2 terms. The T1 terms appear in the subdiagonal, in $T_{\varepsilon_{xz} f_x}$ and $T_{\varepsilon_{yz} f_y}$. These T1 terms serve their purpose, as they are the reason that the matrix is nonsingular for $\Omega = 0$. Looking at the TFM columnwise, and column 3 first, we see that the p_n term in line 1 is type T1, and the ε_{xz} and ε_{yz} terms are type T2, and we observe that they are proportional to the x- and y-partial derivatives of the p_n term (in addition to being multiplied by z). The same is true for the other two columns, except for the previously mentioned additional T1 terms on the subdiagonal.

In summary, the TFM can be interpreted as the p_n terms measuring the surface force as directly as possible within the constraints posed by the subsurface location, while the other two sensor signals complement the p_n signal by measuring its x- and y-spatial derivatives.

3.3. The Decoding Solution

3.3.1. The Ideal Case

Ideally, the solution to the problem would be obtained by simply dividing the sensor output by the transfer function in the frequency domain; i.e.,

$$\phi_0(\omega_x, \omega_y, 0) = T^{-1}(\omega_x, \omega_y, z)s(\omega_x, \omega_y, z),$$

where ϕ_0 is the desired surface signal that needs to be calculated during the decoding process (which can be tractions, displacements, or a combination of the two), $T(\omega_x, \omega_y, z)$ is the transfer function, and s is the measured signal. As can be seen from the TFM expressions, the transfer function is a low-pass filter where the high-frequency response goes exponentially to zero as Ω tends to ∞. Therefore, the inverted transfer function will become arbitrarily large for high frequencies. This is very impractical, and will lead to serious errors in real circumstances. To avoid this problem, we instead use regularized solutions, which is a common practice in treating ill-posed problems such as this one. Most regularization problems are formulated as scalar problems; here, however, we need to use multivariate regularization, which happens to be used in specialized problems such as the digital restoration of multichannel images (Galatsanos and Chin 1989; Galatsanos et al. 1991).

3.3.2. The Real Case

In addition to the features of the ideal problem, the real problem involves the unfavorable effects of noise and spatial sampling. Both these effects can be effectively minimized using regularizing agents in the solution, as shown by Tikhonov and Arsenin (1977). One possible way of solving the resulting integral equations is to discretize the integral and put it in the form of a system of linear equations (Rossi et al. 1991; Pati

et al. 1988). A more intuitive way is to construct a regularizing operator in the frequency domain using transfer functions as follows. The solution is obtained as in the ideal case, except for the multiplication factor $\psi(\omega_x, \omega_y, z, \alpha)$, where α is a regularizing parameter, i.e.,

$$\hat{\bar{\phi}}_0(\omega_x, \omega_y) = \psi(\omega_x, \omega_y, z, \alpha) T^{-1}(\omega_x, \omega_y, z) \bar{s}(\omega_x, \omega_y, z),$$

where $\hat{\bar{\phi}}_0$ is an estimate of the surface signal vector (inputs) and $\bar{s}$ is the stimuli (output) vector. One possible family of regularizing operators that can be constructed are weighted-norm filters (Tikhonov and Arsenin 1977; Karayiannis and Venetsanopoulos 1990), which are of the form

$$\psi_{H,\alpha}(\omega_x, \omega_y, z, \alpha) = \left[T^*T + \alpha H\right]^{-1} T^*T,$$

where $H(\omega_x, \omega_y, z)$ is a weighting function to be determined that will depend on the problem at hand, the sampling interval, and the noise characteristics. The solution is then

$$\hat{\phi}_0 = \left[T^*T + \alpha H\right]^{-1} T^*\bar{s}.$$

It is shown by Tikhonov and Aresnin (1977) and in further detail by Karayiannis and Venetsanopoulos (1990) that in the case of scalar signals, this regularizing agent corresponds to the minimization of a functional. This generalizes readily in the vector case to the functional

$$M_\alpha[\phi_0, s, \alpha] = \int_{-\infty}^{\infty}\int_{-\infty}^{\infty} [T\phi_0 - s]^T [T\phi_0 - s]\, d\omega_x d\omega_y + \alpha \int_{-\infty}^{\infty}\int_{-\infty}^{\infty} \bar{\phi}_0^*(\omega_x, \omega_y) H(\omega_x, \omega_y, z)\bar{\phi}_0(\omega_x, \omega_y) d\omega_x d\omega_y.$$

This means that in the solution, the frequencies of the solution are weighted by the matrix H.

It is also shown by Tikhonov and Aresnin (1977) and Karayiannis and Venetsanopoulos (1990) how the selection of the parameter α and the matrix H can be optimized further. If we assume additive sensor noise which is uncorrelated with the solution, x, y and load, i.e., $s = s_T + s_N$, then H and α can be specified such that the expected value of the squared difference is minimized; i.e.,

$$E\left[\|\tilde{\phi}_0^H\|^2\right] \text{ where } \tilde{\phi}_0^H \triangleq \hat{\phi}_0^H - \phi_0^s,$$

where ϕ_0^s is the uncontaminated signal. The solution to this problem is the *multivariate Wiener inverse* used in problems that appear in digital restoration of multichannel images. It is shown by Galatsanos and colleagues (Galatsanos and Chin 1989; Galatsanos et al. 1991) that in the multivariate case it is

$$H(\omega_x, \omega_y, z) = \frac{1}{\alpha} P_s^{-1}(\omega_x, \omega_y) P_n(\omega_x, \omega_y, z),$$

where $P_s(\omega_x, \omega_y, z)$ is the power-spectrum matrix of the solution, and $P_n(\omega_x, \omega_y)$ is the power-spectrum matrix of the sensor noise. The multivariate Wiener inverse then finally becomes

$$\hat{\bar{\phi}}_0^w = \left[P_s T^*T + P_n\right]^{-1} P_s T^* s. \tag{5}$$

The need for the power spectrum of the solution indicates that the solution is not in a closed form. This problem can be circumvented in several ways. First, the power spectrum can be put equal to qI, where I is the identity matrix and q is a constant, indicating that nothing is known about the solution a priori, and the solution is therefore assumed to be white noise. Second, the solution can be iterated. Third, all prior information about the solution that can be included in a power spectrum can be used there. For example, suppose Coulomb's law of friction applies at all points at the contact interface, and the coefficient of friction is known. The solution can then be constrained to satisfy Coulomb's law by explicitly expressing the correlation between the normal and the tangential tractions in the components of the P_s matrix. Let us further assume that it is known that the object is sliding over the surface but the direction of motion in the (x, y)-plane is unknown; then the power-spectrum matrix would be of the form

$$P_s = \begin{bmatrix} \mu_f^2 & 0 & \mu_f \\ 0 & \mu_f^2 & \mu_f \\ \mu_f & \mu_f & 1 \end{bmatrix} P_{f_z},$$

where P_{f_z} is the power spectrum of f_z, and μ_f is the friction coefficient between the object and the surface. Using this P_s in eq. (5) will constrain the solution to satisfy Coulomb's law; i.e., $f_x = \mu_f f_z$ and $f_y = \mu_f f_z$.

REMARK 3. The linear filter presented here is based on the assumption that the noise properties are shift-invariant and uncorrelated with the input signal. Also, its optimality is achieved with respect to a Euclidean norm functional. The shift-invariance assumption comes naturally with our formulation of the encoding problem as a contact problem on the homogeneous semi-infinite half-space. However, if needed, the Wiener filter can be extended to correctly treat cases when the input and the noise are correlated (Brown and Hwang 1992). Finally, different cost functionals can be prescribed, such as absolute value, p-norm, and maximum entropy (Castleman 1979). These filters should be considered when the Wiener filter has proven inadequate. The details of their construction is hence considered to be a matter of implementation, and beyond the scope of this paper.

4. Identification of Shape and the Onset of Slip: An Illustrative Example

In this section, we present an example that implements the theory discussed above which brings together contact mechanics and tactile sensing. The simulations have two main

objectives: shape identification and detection of the slip onset. In both cases, we will (1) show the necessity and usefulness of the full 3-D formulation presented here, especially in the context of a pseudodynamic problem with mixed-boundary conditions, and (2) show the necessity of the multivariate regularizing inverse in the solution of the decoding problem.

The example problem chosen is that of the incipient relative sliding of two elastic bodies in contact. This problem is particularly interesting in the context of haptics, as the identification of object shape and the prediction of the onset of and the prevention of slip are fundamental issues for both human and robotic exploration and manipulation. It has also been observed by Salisbury and Hills (1983a, 1983b) that objects of general shape will have qualitatively similar behavior as spherical objects, and hence the results presented here will extend to general objects. It is worth noting that this is a mixed boundary-value problem, and is an example of case 4 discussed in Section 2.3. The problem demonstrated here is the indentation of an infinite half-space by an object shaped as a paraboloid, with simultaneous tangential (F_{x_0}, F_{y_0}) and normal (F_{z_0}) load. Assuming Coulomb friction with friction coefficient μ_f, the condition for local slip can be expressed as

$$\mu_f f_z(x,y) \begin{cases} \leq & \sqrt{f_x^2(x,y) + f_y^2(x,y)} \\ \Rightarrow & \text{no slip,} \\ & \\ > & \sqrt{f_x^2(x,y) + f_y^2(x,y)} \\ \Rightarrow & \text{slip occurs.} \end{cases} \tag{6}$$

It is shown by Johnson (1985) that the unique solution to this problem is that local slip occurs on the outer edge of the contact area $c \leq r \leq a$, with $r = \sqrt{x^2 + y^2}$, where

$$\frac{c}{a} = \left[1 - \frac{\sqrt{F_{x_0}^2 + F_{y_0}^2}}{\mu_f F_{z_0}} \right]^{1/3} \tag{7}$$

is the relative size of the nonslip region, and no slip occurs for $r < c$ (see Fig. 13). The resulting surface tractions can be determined using the analytical solution (Johnson 1985) as

$$f_z(x,y) = \frac{F_{z_0}}{\pi a^2} \sqrt{1 - \frac{r^2}{a^2}} \quad \text{for } 0 \leq r \leq a,$$

$$f_t(x,y) = \begin{cases} \dfrac{\mu_f F_{z_0}}{\pi a^2} \sqrt{1 - \dfrac{r^2}{a^2}} \\ \text{where } c \leq r \leq a, \\ \dfrac{\mu_f F_{z_0}}{\pi a^2} \sqrt{1 - \dfrac{r^2}{a^2}} - \dfrac{c}{a} \dfrac{F_{z_0}}{\pi a^2} \sqrt{1 - \dfrac{r^2}{c^2}} \\ \text{where } r < c, \end{cases}$$

where $f_t = f_z = 0$ for $r > a$, and $f_t(x,y)$ is directed along $[F_{x_0}, F_{y_0}]^T$ with $f_t(x,y) = \sqrt{f_x^2(x,y) + f_y^2(x,y)}$.

4.1. *Identification of Shape*

We use here the optimal sensor combination obtained in Section 3.2.2, and hence the encoding part consists of predicting the sensor signal set $(\frac{3}{2E} p_n, \varepsilon_{xz}, \varepsilon_{yz})$ by using the traction vector f above with the TFM, T_{sf} given in eq. (4). The form of these sensor signals is shown in Figures 8a–8c. The decoding part consists of reconstructing the traction and the displacement vectors, from noise-contaminated sensor signals. The displacements will give us the shape of the object where it is in contact with the surface, but that is by definition where the traction is nonzero; hence both displacements and tractions are needed for object-shape identification. For the indicated region, 32×32 samples were used over a 10-mm×10-mm grid with a sensor spacing of 0.4 mm both in the x- and y-directions. It was found that a smaller sensor density introduced aliasing error. The sensor depth was 1 mm. Increasing the sensor depth led to an attenuating effect on the signal, especially at higher frequencies, making them harder to reconstruct.

We will now illustrate the necessity of regularization in the decoding algorithm by adding noise to the sensor signals. In this example, we use a high-pass-filtered Gaussian noise with a signal-to-noise ratio of 11 dB. We observed, however, that the regularization worked satisfactorily for much higher noise levels as well. In Figures 8d–8f, we show the resulting noise-contaminated sensor signals. Profiles of an unregularized solution obtained by inverting T_{sf} in eq. (4) is shown in Figure 9, and profiles of a regularized solution obtained using the Wiener inverse given in eq. (5) is shown in Fig. 10. Since the proposed method of using the Wiener inverse utilizes the known structure of the noise, it may be expected to perform better than that proposed by Ellis and Qin (1994).

Plots of the distributions of displacements are shown in Figure 11, and those of surface tractions in Figure 12. We observe that the regularized inverse is quite close to the uncontaminated solution, but the unregularized one is not recognizable. The locus of points where the forces are nonzero is the contact region, and u_z in that region gives the object shape in contact with the skin (see Figs. 10–12).

4.2. *Onset of Slip*

We will now illustrate how the static solution described in this paper can also be useful in a pseudodynamic problem such as the estimation of onset of slip. For the sake of simplicity, we will consider the case where the normal load F_{zz} is held constant. As the total tangential load, $F_{t_0} = \sqrt{F_{x_0}^2 + F_{y_0}^2}$, takes increasing values, the size of the nonslip region decreases, and when $F_{t_0} = \mu_f F_{z_0}$, global slip will occur. Therefore, knowing the relative size of the nonslip region will enable us to estimate how close a particular loading situation is to slipping. The size of the nonslip region can be inferred from the tangential traction distribution, as there will be a sharp edge

(a) Noise free sensor signal p_n (b) Noise free sensor signal ε_{xz} (c) Noise free sensor signal ε_{yz}

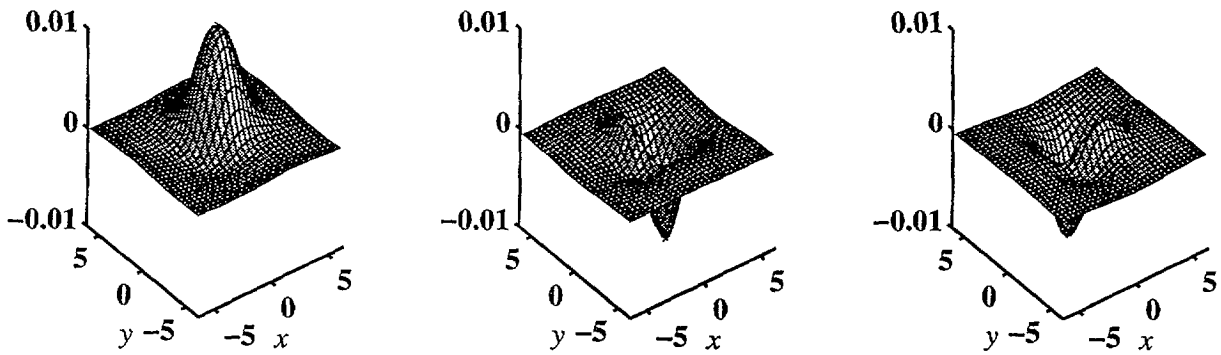

(d) Real sensor signal p_n (e) Real sensor signal ε_{xz} (f) Real sensor signal ε_{yz}

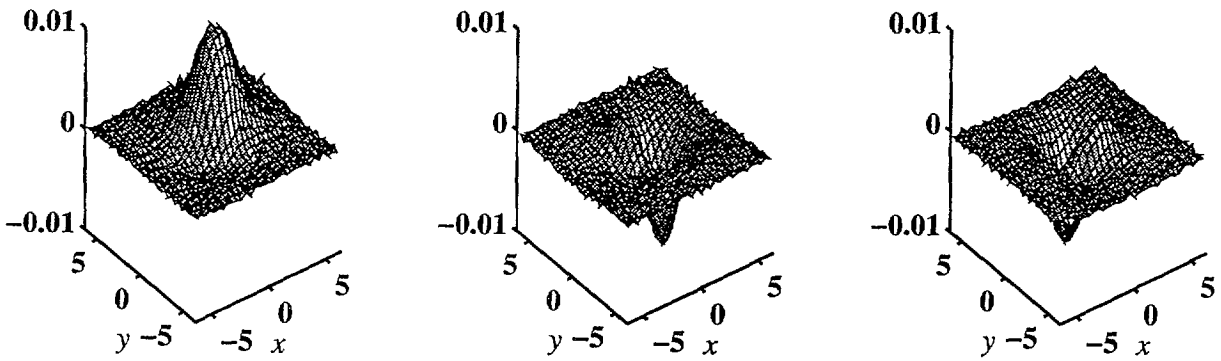

Fig. 8. Sensor signals with and without noise. (a), (b), and (c) indicate p_n, ε_{xz}, ε_{yz} in the noise-free case, respectively; (d), (e), and (f) indicate p_n, ε_{xz}, ε_{yz} in the presence of noise, respectively.

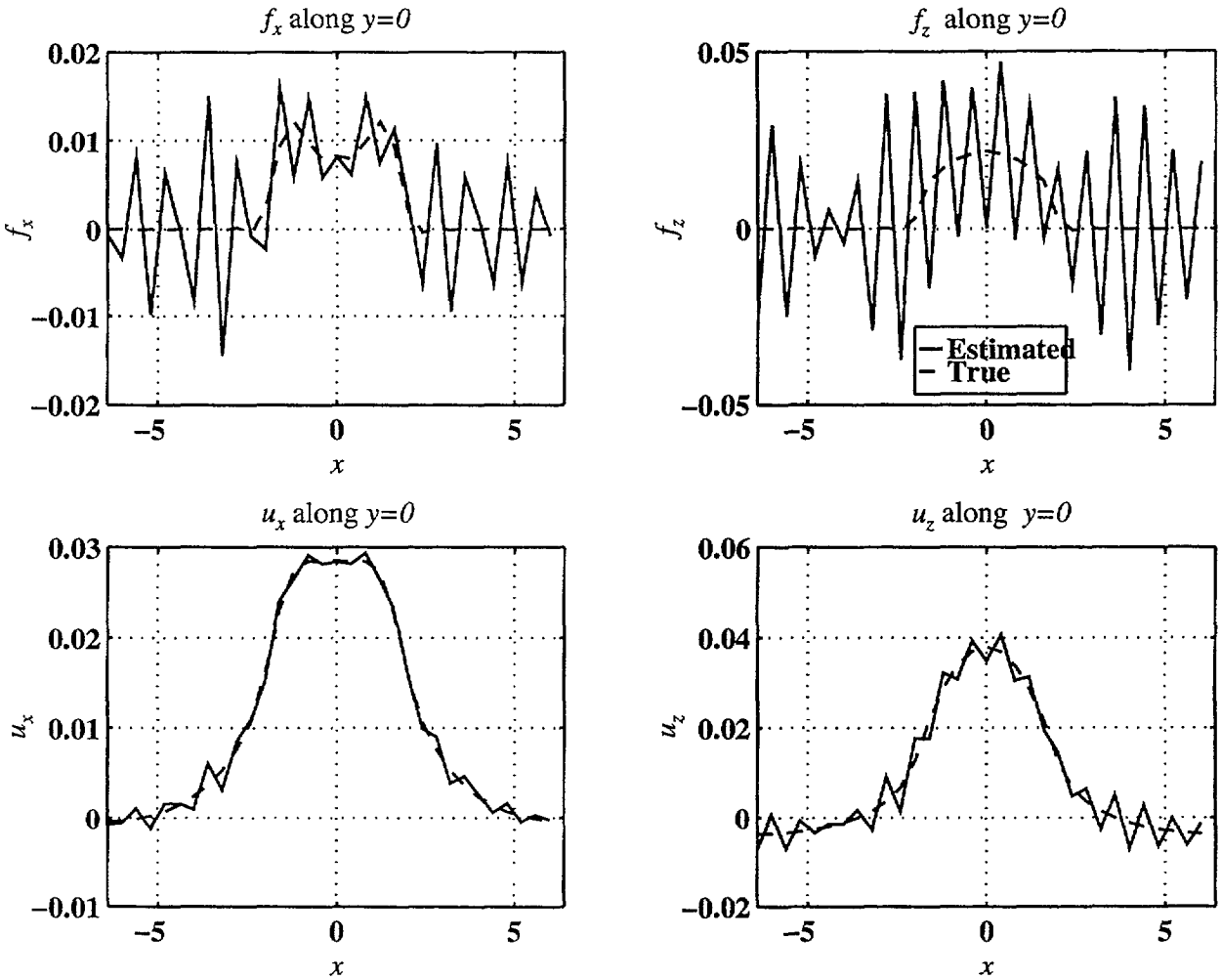

Fig. 9. Profiles of solutions f_x, f_z, u_x, and u_z along $y = 0$ to the decoding problem obtained using an unregularized inverse. We observe that the tractions are hardly recognizable, although the solutions for the displacements, u_x and u_z, are closer to the true solution than are f_x and f_z.

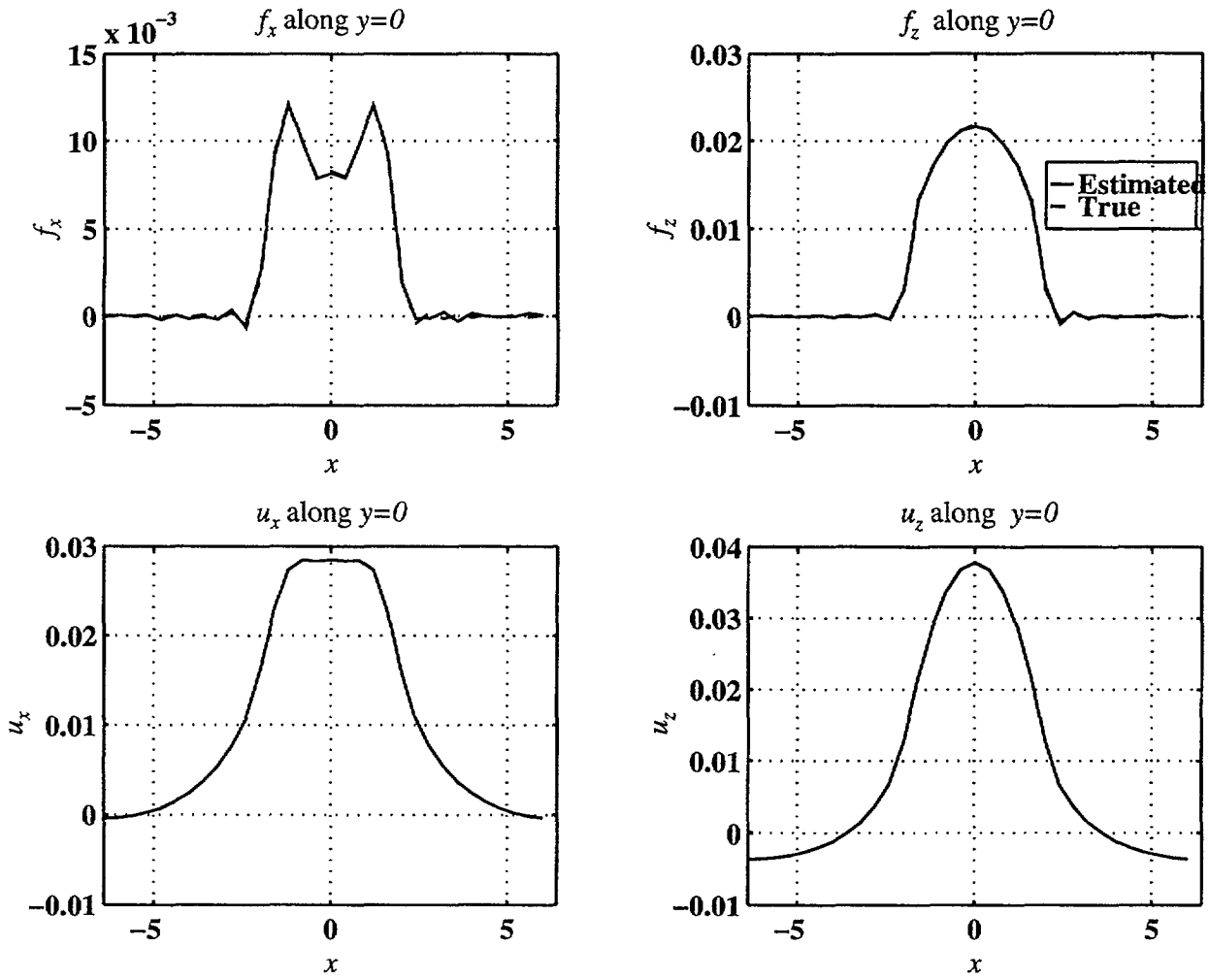

Fig. 10. Profiles of solutions to the decoding problem obtained using the regularized Wiener inverse. We observe that it coincides almost everywhere with the true solution, and that the error is therefore small.

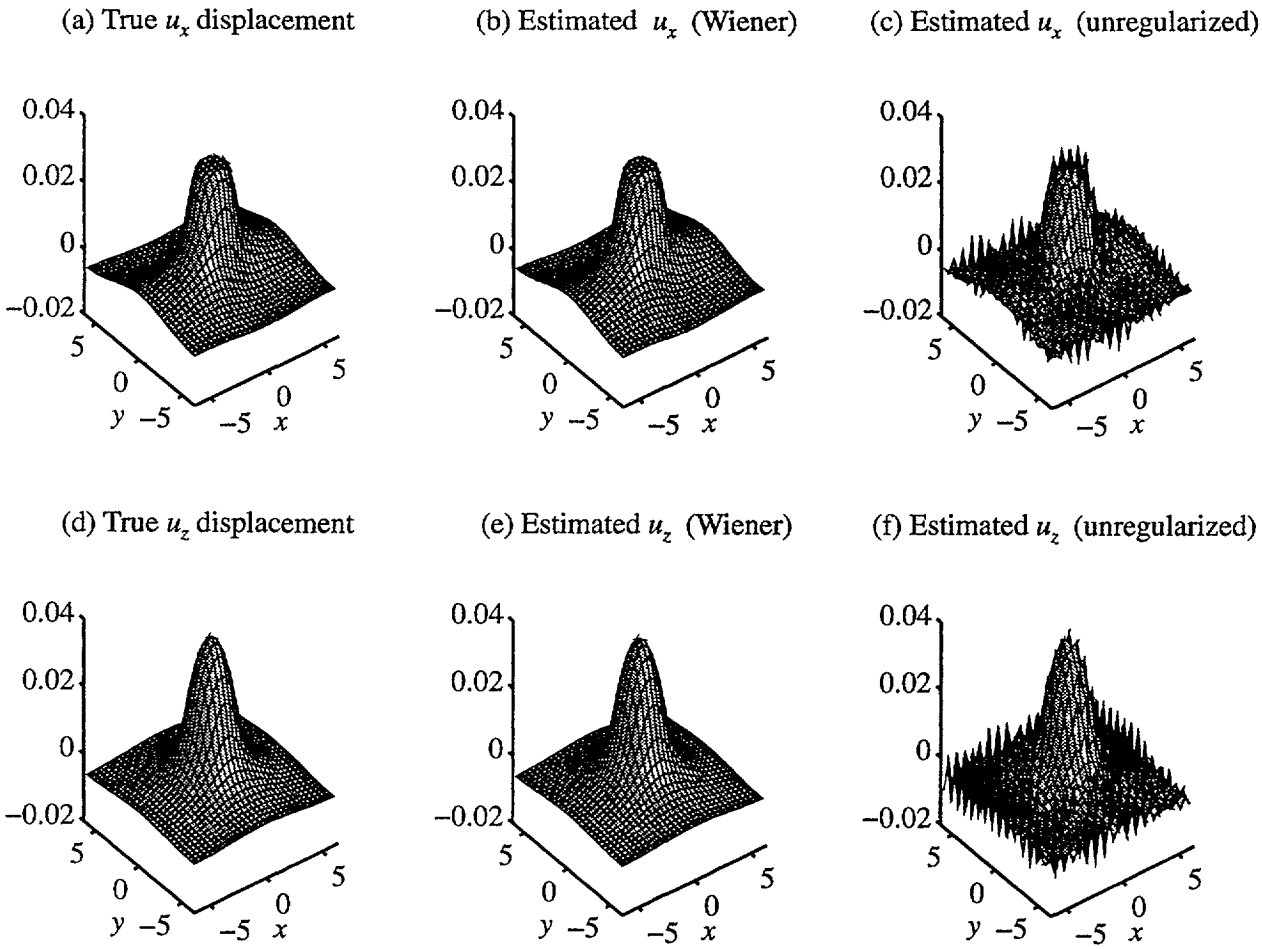

Fig. 11. Surface plots of decoded surface displacements: (a)–(c) u_x; and (d)–(f) u_z. As in Figures 9 and 10, we observe that the true solution and the solution obtained using the Wiener inverse look very similar, but the solution obtained using an unregularized inverse is considerably worse.

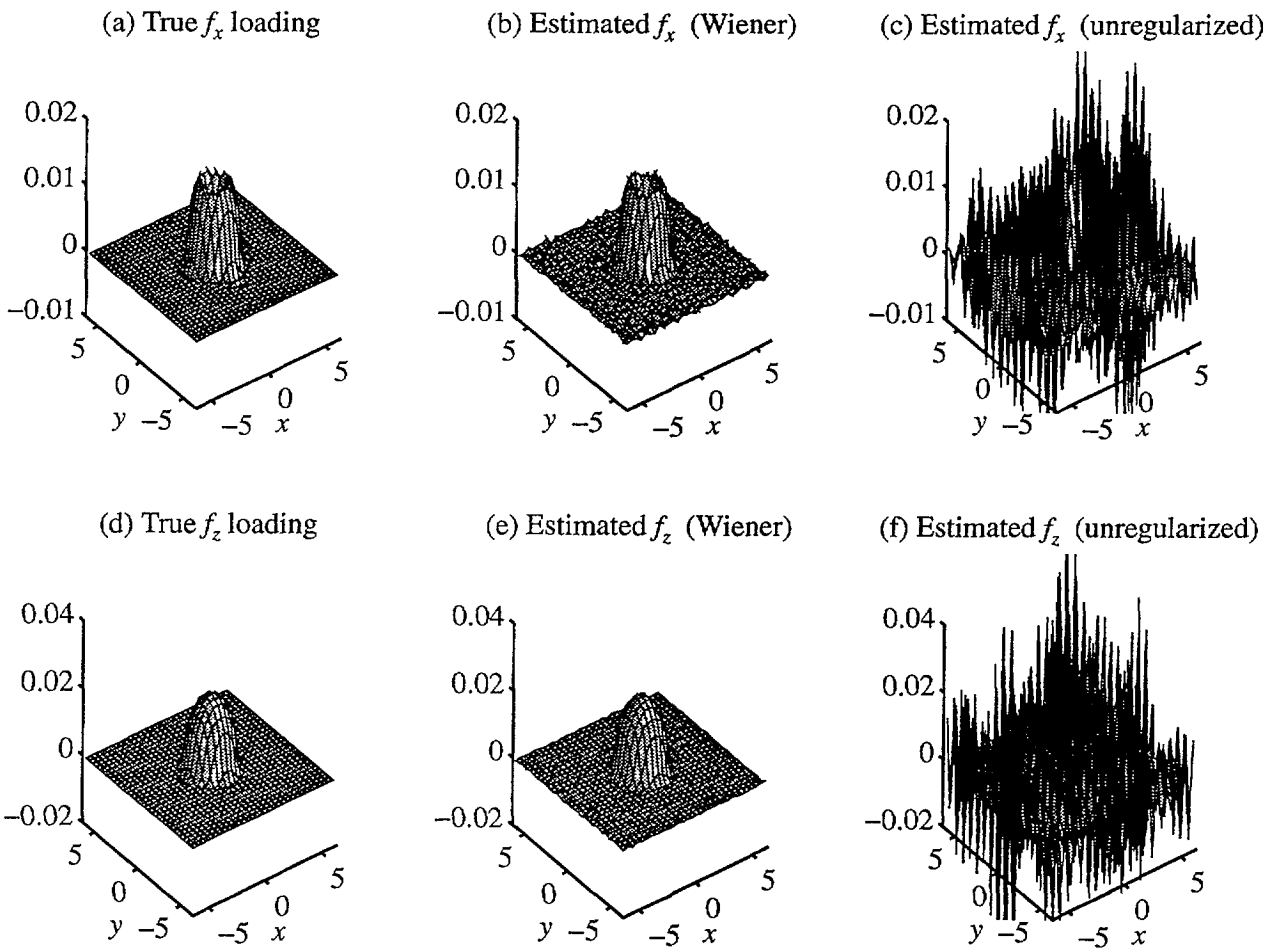

Fig. 12. Surface plots of decoded surface-load distributions: (a)–(c) f_x; and (d)–(f) f_z. Again observe that the true solution and the solution obtained using the Wiener inverse look very similar, but the solution obtained using an unregularized inverse is mostly noise.

along $r = c$ in that distribution. This edge can be seen as two peaks on the 2-D profile plot of $f_x(x, y)$ in Figure 9, and as an edge in the f_x-surface plot in Figure 12. We can measure the radii a and c from the reconstructed $f_x(x, y)$ with the help of standard edge-detecting techniques. That information, along with the total tangential and normal loads, F_{t_0} and F_{z_0}, can either be used in eq. (7) to solve for μ_f or compared to the line plot in Figure 13 to estimate how close the contact is to global slip. For example, we see from Figure 13 that if $c = 0.5a$, then the tangential load has reached 87.5% of its maximum value ($F_{t_0} = 0.875\mu_f F_{z_0}$).

5. Conclusions

In this paper, we have delineated a basic computational theory of haptics that is common to humans and robots. The tactile-identification problem is separated into the encoding and decoding problems, and solutions for both are given. Analysis of the results is shown to lead to a unique and optimal combination of sensors suitable for tactile sensing. An optimized multivariate-regularizing algorithm for the solution of the decoding problem is also presented. From simulations, it is shown how the formulation used here can be applied to predict the onset of slip using tactile sensors. The conclusions of this paper can thus be summarized as follows:

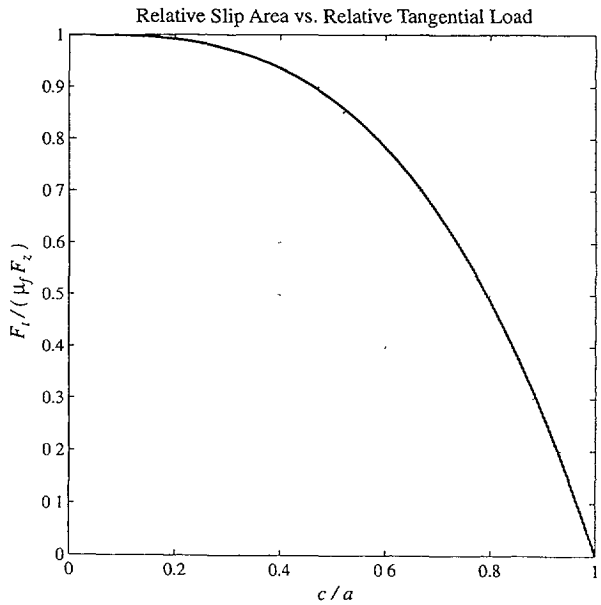

Fig. 13. The relation between the relative tangential load $F_{t_0}/(\mu_f F_{z_0})$, where $F_{t_0} = (F_{x_0}^2 + F_{y_0}^2)^{1/2}$, and the relative no-slip radius $c/a = 1 - F_{t_0}^3/(\mu_f F_{z_0})^3$. As an example, this relation indicates that when the no-slip radius is equal to half the contact radius ($c/a = 1/2$), $F_{t_0} = 0.875\mu_f F_{z_0}$, or the tangential load is 87.5% of the maximum tangential load.

1. To successfully decode a general tactile 3-D signal from a tactile sensor array, a minimum of three independent sensors are needed; $(p_n, \varepsilon_{xz}, \varepsilon_{yz})$ is a unique combination of stress-strain sensory signals which do not have a directional bias.
2. The transfer-function approach developed here allows us to look at the qualitative properties and behavior of the solution, irrespective of the exact form of the load or object shape.
3. The two items above lead to the TFM formulation, a convenient and compact formulation that is well known in control theory. The decoding problem is then reduced, essentially, to the inversion of the TFM.
4. Since the inversion is ill-posed in the presence of noise and discrete sampling, regularization is needed, for which the multivariate Wiener inverse exists as a standard tool.
5. Simulations presented in Section 4 show that the above can be used to calculate surface shape, load distribution, and contact area, and further, to estimate the onset of slip.

Appendix: Derivation of Static Transfer Function Matrices

We start with the differential equations of equilibrium[1]

$$\sigma_{ij,j} = 0 \quad i, j = x, y, z, \tag{8}$$

and the linear stress-strain relations according to Hooke's law

$$\sigma_{ij} = \lambda\varepsilon_{ij}\delta_{ij} + 2\mu\varepsilon_{ij} \quad i, j = x, y, z, \tag{9}$$

where

$$\varepsilon_{ij} = \frac{1}{2}\left(u_{i,j} + u_{j,i}\right) \quad i, j = x, y, z$$

and $\delta_{ij} = 1$ if and only if $i = j$, and is zero otherwise. Further, the Lamè constants λ and μ (shear modulus) are in terms of Young's modulus and the Poisson ratio,

$$\lambda = \frac{\nu E}{(1+\nu)(1-2\nu)}, \quad \mu = \frac{E}{2(1+\nu)}.$$

To solve these nine partial differential equations, we make use of the two-dimensional Fourier transform defined by Bracewell (1978):

$$\bar{f}(\omega_x, \omega_y) = \int_{-\infty}^{+\infty}\int f(x, y)e^{-j(\omega_x x + \omega_y y)}\mathrm{d}x\mathrm{d}y$$

$$f(x, y) = \frac{1}{4\pi^2}\int_{-\infty}^{+\infty}\int \bar{f}(\omega_x, \omega_y)e^{j(\omega_x x + \omega_y y)}\mathrm{d}\omega_x\mathrm{d}\omega_y.$$

1. Here we use tensor notation for compactness, where a "$, j$" in a subscript means a partial derivative with respect to the independent variable represented by j, and repeated symbols in a subscript stand for summation over all indices.

Assuming that all integrals are well behaved as $|x, y| \to \infty$, we apply this transform to each term in the statements in eqs. (8) and (9). Then the operator $\frac{\partial}{\partial x}$ is replaced by multiplication by $j\omega_x$, and $\frac{\partial}{\partial y}$ by $j\omega_x$. We further use D to notate $\frac{\partial}{\partial z}$. The nine partial differential equations have now been transformed into ordinary differential equations in D ($\frac{\partial}{\partial z}$ becomes $\frac{\mathrm{d}}{\mathrm{d}z}$). Denoting

$$\gamma_{ij} = 2\varepsilon_{ij} \qquad \text{for } i \neq j, \tag{10}$$

we write eqs. (8) and (9) using matrix-vector notation as

$$K^T\bar{\sigma} = 0, \quad \bar{\gamma} = K\bar{u},$$

and

$$\bar{\sigma} = C\bar{\gamma},$$

where

$$K^T = \begin{bmatrix} j\omega_x & 0 & 0 & j\omega_y & D & 0 \\ 0 & j\omega_y & 0 & j\omega_x & 0 & D \\ 0 & 0 & D & 0 & j\omega_x & j\omega_y \end{bmatrix},$$

$$C = \begin{bmatrix} \lambda+2\mu & \lambda & \lambda & 0 & 0 & 0 \\ \lambda & \lambda+2\mu & \lambda & 0 & 0 & 0 \\ \lambda & \lambda & \lambda+2\mu & 0 & 0 & 0 \\ 0 & 0 & 0 & \mu & 0 & 0 \\ 0 & 0 & 0 & 0 & \mu & 0 \\ 0 & 0 & 0 & 0 & 0 & \mu \end{bmatrix},$$

$\bar{\sigma} = \left[\bar{\sigma}_{xx}, \bar{\sigma}_{yy}, \bar{\sigma}_{zz}, \bar{\sigma}_{xy}, \bar{\sigma}_{xz}, \bar{\sigma}_{yz}\right]^T$, and $\bar{\gamma} = \left[\bar{\varepsilon}_{xx}, \bar{\varepsilon}_{yy}, \bar{\varepsilon}_{zz}, \bar{\gamma}_{xy}, \bar{\gamma}_{xz}, \bar{\gamma}_{yz}\right]^T$. Here, the notation in eq. (10) is used for the sake of simplicity in the definition of K. Eliminating $\bar{\sigma}$ and $\bar{\varepsilon}$, we get

$$K^TCK\bar{u} = 0, \tag{11}$$

where $\bar{u} = \left[\bar{u}_x, \bar{u}_y, \bar{u}_z\right]^T$, and

$$K^TCK = \begin{bmatrix} D^2-\Omega^2-\omega_x^2(\beta^2-1) & -\omega_x\omega_y(\beta^2-1) & j\omega_x(\beta^2-1)D \\ -\omega_x\omega_y(\beta^2-1) & D^2-\Omega^2-\omega_y^2(\beta^2-1) & j\omega_y(\beta^2-1)D \\ j\omega_x(\beta^2-1)D & j\omega_y(\beta^2-1)D & \beta^2(D^2-\Omega^2)+\Omega^2\beta^2 \end{bmatrix},$$

with $\Omega^2 = \omega_x^2 + \omega_y^2$ and $\beta^2 = (\lambda+2\mu)/\mu$. The determinant of this matrix is

$$\det(K^TCK) = \beta^2\mu^3\left[D^2-\Omega^2\right]^3,$$

and this system therefore has nontrivial solutions of the form

$$\bar{u}_i = (A_i + B_iz + C_iz^2)e^{-\Omega z} \quad i = x, y, z,$$

where A_i, B_i, C_i are independent of z, and we have also used the condition that displacements stay finite as $z \to \infty$ to include only terms with negative exponents. Substituting this back into eq. (11), we obtain

$$\begin{aligned} A_z &= \frac{1}{\Omega}\left(j\omega_xA_x + j\omega_yA_y + B_z\frac{\beta^2+1}{\beta^2-1}\right), \\ B_x &= -\frac{j\omega_x}{\Omega}B_z, \\ B_y &= -\frac{j\omega_y}{\Omega}B_z, \\ C_x &= C_y = C_z = 0, \end{aligned}$$

which gives

$$\begin{bmatrix} \bar{u}_x \\ \bar{u}_y \\ \bar{u}_z \end{bmatrix} = e^{-\Omega z}\begin{bmatrix} 1 & 0 & -\frac{j\omega_xz}{\Omega} \\ 0 & 1 & -\frac{j\omega_yz}{\Omega} \\ \frac{j\omega_x}{\Omega} & \frac{j\omega_y}{\Omega} & \frac{1}{\Omega}\frac{\beta^2+1}{\beta^2-1}+z \end{bmatrix}\begin{bmatrix} A_x \\ A_y \\ B_z \end{bmatrix}. \tag{12}$$

The three still-unknown terms, A_x, A_y, and B_z, will be determined by boundary conditions at $z = 0$. Here, we will first pose the boundary conditions in terms of the load distributions on the surface of the infinite half-space, defined by $z \geq 0$. The z-normal stress σ_{zz} at the surface $z = 0$ equals normal load on the surface, f_z. Similarly, the shear stresses σ_{xz} and σ_{yz} at $z = 0$ equal the shear loads on the same surface, f_x and f_y, respectively. The relevant stresses can be derived by substituting eq. (12) into eq. (9), which become

$$\begin{bmatrix} \bar{\sigma}_{xz} \\ \bar{\sigma}_{yz} \\ \bar{\sigma}_{zz} \end{bmatrix} = \frac{\mu e^{-\Omega z}}{\Omega}\begin{bmatrix} -(2\omega_x^2+\omega_y^2) & -\omega_x\omega_y & 2j\omega_x\left(\frac{1}{\beta^2-1}+\Omega z\right) \\ -\omega_x\omega_y & -(\omega_x^2+2\omega_y^2) & 2j\omega_y\left(\frac{1}{\beta^2-1}+\Omega z\right) \\ j\omega_x\Omega & j\omega_y\Omega & \Omega\left(\frac{\beta^2}{\beta^2-1}+\Omega z\right) \end{bmatrix}\begin{bmatrix} A_x \\ A_y \\ B_z \end{bmatrix}. \tag{13}$$

The unknown terms A_x, A_y, and B_z can then be found by letting $z = 0$ and either invert eq. (12) with $[\bar{u}_x, \bar{u}_y, \bar{u}_z] = [\bar{u}_{x0}, \bar{u}_{y0}, \bar{u}_{z0}]$ or eq. (13) with $[\bar{\sigma}_{xz}, \bar{\sigma}_{yz}, \bar{\sigma}_{zz}] = [\bar{f}_x, \bar{f}_y, \bar{f}_z]$.

Transfer-Function Matrices (TFMs) for Tractions as Inputs

It is convenient to solve for each load case separately and state the solution in terms of a TFM, which after we have substituted for β and μ, finally becomes

$$\bar{u} = T_{uf}\bar{f},$$

with

$$T_{uf} = \frac{e^{-z\Omega}}{2\mu\Omega^3}\begin{bmatrix} 2\Omega^2 - \omega_x^2(2\nu+\Omega z) & -\omega_x\omega_y(2\nu+\Omega z) & j\omega_x\Omega(1-2\nu-\Omega z) \\ -\omega_x\omega_y(2\nu+\Omega z) & 2\Omega^2 - \omega_y^2(2\nu+\Omega z) & j\omega_y\Omega(1-2\nu-\Omega z) \\ -j\omega_x\Omega(1-2\nu+\Omega z) & -j\omega_y\Omega(1-2\nu+\Omega z) & (2(1-\nu)+\Omega z)\Omega^2 \end{bmatrix}. \tag{14}$$

The strain and the stress field TFMs are obtained using the relations in eq. (9) and results in

$$\bar{\varepsilon} = T_{\varepsilon f}\bar{f}, \quad \text{where,} \quad \bar{\varepsilon} = [\varepsilon_{xx}, \varepsilon_{yy}, \varepsilon_{zz}, \varepsilon_{xy}, \varepsilon_{xz}, \varepsilon_{yz}]^T,$$

with

$$T_{\varepsilon f} = \frac{e^{-z\Omega}}{2\mu\Omega^3}\begin{bmatrix} j\omega_x(2\Omega^2 - \omega_x^2(2\nu+\Omega z)) & -j\omega_x^2\omega_y(2\nu+\Omega z) & -\Omega\omega_x^2(1-2\nu-\Omega z) \\ -j\omega_x\omega_y^2(2\nu+\Omega z) & j\omega_y\left(2\Omega^2 - \omega_y^2(2\nu+\Omega z)\right) & -\Omega\omega_y^2(1-2\nu-\Omega z) \\ -j\Omega^2\omega_x(2\nu-\Omega z) & -j\Omega^2\omega_y(2\nu-\Omega z) & -\Omega^3(1-2\nu+\Omega z) \\ j\omega_y(\Omega^2 - \omega_x^2(2\nu+\Omega z)) & j\omega_x\left(\Omega^2 - \omega_y^2(2\nu+\Omega z)\right) & -\Omega\omega_x\omega_y(1-2\nu-\Omega z) \\ -\Omega^2(\Omega - \omega_x^2 z) & \Omega^2\omega_x\omega_y z & j\Omega^3\omega_x z \\ \Omega^2\omega_x\omega_y z & -\Omega^2(\Omega - \omega_y^2 z) & j\Omega^3\omega_y z \end{bmatrix}, \tag{15}$$

and

$$\bar{\sigma} = T_{\sigma f}\bar{f},$$

where

$$\bar{\sigma} = [\sigma_{xx}, \sigma_{yy}, \sigma_{zz}, \sigma_{xy}, \sigma_{xz}, \sigma_{yz}]^T,$$

with

$$T_{\sigma f} = \frac{e^{-z\Omega}}{\Omega^3}\begin{bmatrix} j\omega_x\left(2\Omega^2 + 2\nu\omega_y^2 - \omega_x^2 z\Omega\right) & j\omega_y\left(2\nu\omega_y^2 - \omega_x^2 z\Omega\right) & -\Omega\left(2\nu\omega_y^2 + \omega_x^2(1-\Omega z)\right) \\ j\omega_x\left(2\nu\omega_x^2 - \Omega\omega_y^2 z\right) & j\omega_y\left(2\Omega^2 + 2\nu\omega_x^2 - \omega_y^2 z\Omega\right) & -\Omega\left(2\nu\omega_x^2 + \omega_y^2(1-\Omega z)\right) \\ j\Omega^3\omega_x z & j\Omega^3\omega_y z & -\Omega^3(1+z\Omega) \\ j\omega_y\left(\Omega^2 - \omega_x^2(2\nu+z\Omega)\right) & j\omega_x\left(\Omega^2 - \omega_y^2(2\nu+z\Omega)\right) & -\Omega\omega_x\omega_y(1-2\nu-z\Omega) \\ -\Omega^2\left(\Omega - \omega_x^2 z\right) & \Omega^2\omega_x\omega_y z & j\Omega^3\omega_x z \\ \Omega^2\omega_x\omega_y z & -\Omega^2\left(\Omega - \omega_y^2 z\right) & j\Omega^3\omega_y z \end{bmatrix}. \tag{16}$$

We also calculate the TFM for the mean normal stress, and defined as

$$p_n = \frac{1}{3}(\sigma_x + \sigma_y + \sigma_z),$$

which gives

$$\bar{p}_n = T_{p_n f}\bar{f},$$

with

$$T_{p_n f} = \frac{2E}{3}\frac{e^{-z\Omega}}{2\mu\Omega}\begin{bmatrix} j\omega_x & j\omega_y & -\Omega \end{bmatrix}. \tag{17}$$

The relationship between $\bar{u}_0$ and $\bar{f}$ can be found by letting $z = 0$ in eq. (14), obtaining

$$\bar{u}_0 = T_{u_0 f}\bar{f},$$

with

$$T_{u_0 f} = \frac{1}{2\mu\Omega^3}\begin{bmatrix} 2(\Omega^2 - \nu\omega_x^2) & -2\nu\omega_x\omega_y & j(1-2\nu)\omega_x\Omega \\ -2\nu\omega_x\omega_y & 2(\Omega^2 - \nu\omega_y^2) & j(1-2\nu)\omega_y\Omega \\ -j(1-2\nu)\omega_x\Omega & -j(1-2\nu)\omega_y\Omega & 2(1-\nu)\Omega^2 \end{bmatrix}. \tag{18}$$

We note that the z-component decouples from the x- and y-components when the material is incompressible ($\nu = 0.5$).

TFMs for Displacements as Inputs

When the surface displacements are considered as the inputs, the TFMs are found similarly as the ones in the previous section:

$$\bar{f} = T_{fu_0}\bar{u}_0,$$

with

$$T_{fu_0} = \frac{\mu}{(3-4\nu)\Omega}$$

$$\begin{bmatrix} \Omega^2(3-4\nu)+\omega_x^2 & \omega_x\omega_y & 2j(1-2\nu)\omega_x\Omega \\ \omega_x\omega_y & \Omega^2(3-4\nu)+\omega_y^2 & 2j(1-2\nu)\omega_y\Omega \\ 2j(1-2\nu)\omega_x\Omega & 2j(1-2\nu)\omega_y\Omega & 4(1-\nu)\Omega^2 \end{bmatrix}, \quad (19)$$

$$\bar{u} = T_{uu_0}\bar{u}_0,$$

and

$$T_{uu_0} = \frac{e^{-z\Omega}}{(3-4\nu)\Omega}$$

$$\begin{bmatrix} (3-4\nu)\Omega-\omega_x^2 z & -\omega_x\omega_y z & -j\omega_x\Omega z \\ -\omega_x\omega_y z & (3-4\nu)\Omega-\omega_y^2 z & -j\omega_y\Omega z \\ -j\omega_x\Omega z & -j\omega_y\Omega z & (3-4\nu)\Omega+\Omega^2 z \end{bmatrix}. \quad (20)$$

For the strains

$$\bar{\varepsilon} = T_{\varepsilon u_0}\bar{u}_0,$$

with

$$T_{\varepsilon u_0} = \frac{e^{-z\Omega}}{(3-4\nu)\Omega} \times$$

$$\begin{bmatrix} j\omega_x\left((3-4\nu)\Omega-\omega_x^2 z\right) & -j\omega_x^2\omega_y z & \Omega\omega_x^2 z \\ -j\omega_x\omega_y^2 z & j\omega_y\left((3-4\nu)\Omega-\omega_y^2 z\right) & \Omega\omega_y^2 z \\ -j\Omega\omega_x(1-\Omega z) & -j\Omega\omega_y(1-\Omega z) & -\Omega^2(2(1-2\nu)+\Omega z) \\ \frac{j}{2}\omega_y\left((3-4\nu)\Omega-2\omega_x^2 z\right) & \frac{j}{2}\omega_x\left((3-4\nu)\Omega-2\omega_y^2 z\right) & \Omega\omega_x\omega_y z \\ -\frac{1}{2}\left((3-4\nu)\Omega^2+\omega_x^2(1-2\Omega z)\right) & -\frac{1}{2}\omega_x\omega_y(1-2z\Omega) & j\Omega\omega_x(1-2\nu)+\Omega z) \\ -\frac{1}{2}\omega_x\omega_y(1-2z\Omega) & -\frac{1}{2}\left((3-4\nu)\Omega^2+\omega_y^2(1-2\Omega z)\right) & j\Omega\omega_x(1-2\nu)+\Omega z) \end{bmatrix} \quad (21)$$

and for the stresses,

$$\bar{\sigma} = T_{\sigma u_0}\bar{u}_0,$$

with

$$T_{\sigma u_0} = \frac{2\mu e^{-z\Omega}}{(3-4\nu)\Omega} \times$$

$$\begin{bmatrix} j\omega_x\left((3-2\nu)\Omega-\omega_x^2 z\right) & j\omega_y\left(2\nu\Omega-\omega_x^2 z\right) & -\Omega\left(2\nu\Omega-\omega_x^2 z\right) \\ j\omega_x\left(2\nu\Omega-\omega_y^2 z\right) & j\omega_y\left((3-2\nu)\Omega-\omega_y^2 z\right) & -\Omega\left(2\nu\Omega-\omega_y^2 z\right) \\ -j\Omega\omega_x(1-2\nu-\Omega z) & -j\Omega\omega_y(1-2\nu-\Omega z) & -\Omega^2(2(1-\nu)+\Omega z) \\ \frac{j}{2}\omega_y\left((3-4\nu)\Omega-2\omega_x^2 z\right) & \frac{j}{2}\omega_x\left((3-4\nu)\Omega-2\omega_y^2 z\right) & \Omega\omega_x\omega_y z \\ -\frac{1}{2}\left((3-4\nu)\Omega^2+\omega_x^2(1-2\Omega z)\right) & -\frac{1}{2}\omega_x\omega_y(1-2\Omega z) & j\Omega\omega_x(1-2\nu+\Omega z) \\ -\frac{1}{2}\omega_x\omega_y(1-2\Omega z) & -\frac{1}{2}\left((3-4\nu)\Omega^2+\omega_y^2(1-2\Omega z)\right) & j\Omega\omega_y(1-2\nu+\Omega z) \end{bmatrix}. \quad (22)$$

Finally, for the mean normal stress, we obtain

$$\bar{p}_n = T_{p_n u_0}\bar{u}_0,$$

with

$$T_{p_n u_0} = \frac{2E}{3}\frac{e^{-z\Omega}}{(3-4\nu)}\begin{bmatrix} j\omega_x & j\omega_y & \Omega \end{bmatrix}. \quad (23)$$

Acknowledgments

The work reported here was supported by the ONR URI grant N00014-92-J-1814 and by the National Science Foundation under grant ECS-9296070.

References

Bracewell, R. 1978. *The Fourier Transform and Its Applications*. New York: McGraw-Hill.

Brown, R., and Hwang, P. 1992. *Introduction to Random Signals and Applied Kalman Filtering*. New York: Wiley.

Cameron, A., Daniel, R., and Durrant-Whyte, H. 1988 (Philadelphia, PA). Touch and motion. *Proc. of the IEEE Conf. on Robot. and Automat.* Los Alamitos, CA: IEEE, pp. 1062–1067.

Castleman, K. 1979. *Digital Image Processing*. Englewood Cliffs, NJ: Prentice Hall.

Dandekar, K. 1995. Role of mechanics in tactile sensing of shape. Ph.D. thesis, Massachusetts Institute of Technology.

Eason, G., Fulton, J., and Sneddon, I. 1956. The generation of waves in an infinite elastic solid by variable body forces. *Phil. Trans. A.* 248: 548–607.

Ellis, R., and Qin, M. 1994. Singular value and finite-element analysis of tactile shape recognition. *Proc. of the IEEE Intl. Conf. on Robot. and Automat.* Washington, DC: IEEE, pp. 2529–2535.

Fearing, R. 1990. Tactile sensing mechanisms. *Intl. J. Robot. Res.* 9:3–23.

Fearing, R. 1992. Planar elasticity for tactile sensing. In Nicholls, H. R. (ed.): *Advanced Tactile Sensing for Robotics*. World Scientific.

Fearing, R., and Hollerbach, J. 1984. Basic solid mechanics for tactile sensing. *Intl. J. Robot. Res.* 4(3):40–54.

Galatsanos, N., and Chin, R. 1989. Digital restoration of multichannel images. *IEEE Trans. Accoustics, Speech, Signal Processing* 37:415–421.

Galatsanos, N., Katsaggelos, A., Chin, R., and Hillery, A. 1991. Least squares restoration of multichannel images. *IEEE Trans. Signal Processing* 39:2222–2252.

Gladwell, G. 1980. *Contact Problems in the Classical Theory of Elasticity*. Alphen aan den Rijn: Sijthoff and Noordhoff.

Howe, R. D., and Cutkosky, M. R. 1993. Dynamic tactile sensing: Perception of fine surface features with stress rate sensing. *IEEE Trans. Robot. Automat.* 9:140–151.

Jayawant, B. 1989. Tactile sensing in robotics. *J. Physics E: Scientific Instruments* 22:604–692.

Johnson, K. L. 1985. *Contact Mechanics*. Cambridge, UK: Cambridge University Press.

Karayiannis, N., and Venetsanopoulos, A. 1990. Regularizing theory in image restoration—the stabilizing functional approach. *IEEE Trans. Accoustics, Speech, Signal Processing* 38:1155–1179.

Nicholls, H. 1992. Tactile sensor design. In Nicholls, H. R. (ed.): *Advanced Tactile Sensing for Robotics.* London: World Scientific.

Nicolson, E., and Fearing, R. 1993 (Yokohama, Japan). Sensing capabilities of linear elastic cylindrical fingers. *Proc. of the IEEE/RSJ Conf. on Intell. Robots and Sys.* Washington, DC: IEEE, pp. 1062–1067.

Pati, Y., Friedman, D., Krishnaprasad, P., Yao, C., and Peckerar, M. 1988 (Philadelphia, PA). Neural networks for tactile perception. *Proc. of the IEEE Conf. on Robot. and Automat.* Los Alamitos, CA: IEEE, pp. 135–139.

Phillips, J. R., and Johnson, K. O. 1981. Tactile spatial resolution, III: A continuum model of skin-predicting mechanoreceptor responses to bars, edges, and gratings. *J. Neurophysiology* 46:1204–1225.

Rossi, D. D., Caiti, A., Bianchi, R., and Canepa, G. 1991 (Sacramento, CA). Fine-form tactile discrimination through inversion of data from a skin-like sensor. *Proc. of the IEEE Intl. Conf. on Robot. and Automat.*, pp. 398–403.

Salisbury, A., and Hills, D. 1983a. Some useful results in the classical Hertz contact problem. *J. Strain Analysis* 18:101–105.

Salisbury, A., and Hills, D. 1983b. Some useful results in the tangentially loaded Hertzian contact problem. *J. Strain Analysis* 18:107–110.

Shimoga, K. 1992 (Troy, New York). Finger-force and touch-feedback issues in dexterous telemanipulation. *Proc. of the NASA-CIRSSE Intl. Conf. on Intell. Robot. Sys. for Space Explor.*

Shimojo, M. 1997. Mechanical filtering effect of elastic cover for tactile sensor. *IEEE Trans. on Robot. and Automat.* 13(1): 128–132.

Sneddon, I. N. 1951. *Fourier Transforms.* New York: McGraw-Hill.

Sneddon, I. N. 1975. Integral transform methods for the solution of mixed boundary value problems in the classical theory of elastostatics. In *Application of Integral Transforms in the Theory of Elasticity.* Wien: Springer-Verlag.

Speeter, T. 1992. Three-dimensional finite-element analysis of elastic continua for tactile sensing. *Intl. J. Robot. Res.* 11:1–19.

Srinivasan, M. A. 1988. Tactile sensing in humans and robots: Computational theory and algorithms. Technical Report, Newman Laboratory, Department of Mechanical Engineering, Massachusetts Institute of Technology.

Srinivasan, M. A. 1995. Haptic interfaces. In Durlach, N. I., and Mavor, A. S. (eds.): *Virtual Reality: Scientific and Technical Challenges. Report of the Committee on Virtual Reality Research and Development.* Washington DC: National Research Council, National Academy Press.

Srinivasan, M. A., and Dandekar, K. 1996. An investigation of the mechanics of tactile sense using two-dimensional models of the primate fingertip. *J. Biomech. Eng.* 118:48–55.

Tikhonov, A. N., and Arsenin, V. Y. 1977. *Solutions of Ill-Posed Problems.* New York: Wiley.

Ping Li
Yumei Wen

Department of Opto-electronic Precision Instruments
Chongqing University
Chongqing, 400044, People's Republic of China
ymwen@cqu.edu.cn

An Arbitrarily Distributed Tactile-Sensor Array Based on a Piezoelectric Resonator

Abstract

This paper introduces a new principle and real structure of a nonscanning, fast-response, arbitrarily distributed tactile-sensor array using a piezoelectric resonator. The piezoelectric sensor has high stability, and the quasi-digital output can be measured easily and precisely. The sensory position can also be measured quickly and precisely. In addition, the tactile sensor array of soft piezoelectric film is adaptive to the sensitive skin of robot.

1. Introduction

Perception of the external environment and objective state is a very important feature of intelligent robots. It is inevitable that a sensor array is the base of the sense of touch in robotics. A tactile-sensor array acts as human sensory receptors in skin. When an external impulse is applied to the human body, sensory receptors give out sensory signals, and the sensory signals are conducted to the central nervous system along nerve fibers in parallel, so the brain can react as fast as possible. In a sensor array, the usual way to generate an output is scanning; that is, the sensory signal of each element in the array is read in sequence under the control of a designated clock. So if there are a large number of sensory elements and diverse measurands in a sensor array, the response of a tactile-sensor array is not fast (Bicchi, Salisbury, and Brock 1993; Cheung and Lumelsky 1992).

Because of their excellent electromechanical coupling effects, piezoelectric materials have been successfully used as sensory elements. Domenici and Rossi proposed "A stress-component-selective tactile sensor array" (1992), and Morten, Cicco, and Prudenziati introduced a "resonant pressure sensor based on piezoelectric properties of ferroelectric thick film" (1992). In these papers, scanning is selected as the output method of the array sensor, and resonant sensing is utilized for an identical sensor; therefore, these sensors are not adaptable for large-scale and fast tactile-array sensors.

This paper introduces a new principle and structure for a nonscanning, fast-response, arbitrarily distributed, tactile piezoelectric resonant-sensor array. For example, once a pressure or force is applied to the surface of a quartz crystal plane, the quartz resonant frequency in the activation area will change along with the diversity of the applied pressure or force. At the same time, the resonant wave will propagate in all directions within the quartz plane. Four piezoelectric transducers are placed on each corner of the quartz plane to convert mechanical vibration of the plane into an electric form to detect its resonant frequency. The position of the sensing point may be determined from the different code of resonant frequency. The sensing frequency of the quartz resonator has very high precision and stability, and value of force can be computed easily and accurately. The deposited silver film employed as electrodes on both surfaces can be arranged in any shape, making it possible to design a tactile sensor array in any arbitrary shape. The sensory method in an array of this type is very specific, and the output is a quasi-digital signal; thus the output antijam is excellent. Moreover, its transmission and measurement can be digitally conducted directly.

2. Precision Resonant Piezoelectric Sensors Based on Quartz

The resonant frequency of a piezoelectric resonator is very stable. The frequency drift of quartz is over 10^{-6}. Usually, an AT-cut quartz crystal is used to construct a resonant-force sensor, as shown in Figure 1. When force or pressure is applied to a resonant quartz slice, strain will occur on the slice, and the resonant frequency f is given as follows:

$$\Delta f/f = (f - f_0)/f = K \times F, \tag{1}$$

The International Journal of Robotics Research
Vol. 18, No. 2, February 1999, pp. 152-158,